



# Large-scale structures of turbulent Rayleigh–Bénard convection in a slim-box

Cite as: Phys. Fluids **33**, 065103 (2021); <https://doi.org/10.1063/5.0048775>

Submitted: 26 February 2021 • Accepted: 13 April 2021 • Published Online: 01 June 2021

 Wen-Feng Zhou (周文丰) and  Jun Chen (陈军)



View Online



Export Citation



CrossMark

## ARTICLES YOU MAY BE INTERESTED IN

[Significance of near-wall dynamics in enhancement of heat flux for roughness aided turbulent Rayleigh–Bénard convection](#)

Physics of Fluids **33**, 065114 (2021); <https://doi.org/10.1063/5.0053522>

[Phase decomposition analysis on oscillatory Rayleigh–Bénard turbulence](#)

Physics of Fluids **33**, 045108 (2021); <https://doi.org/10.1063/5.0042645>

[Flow states in two-dimensional Rayleigh–Bénard convection as a function of aspect-ratio and Rayleigh number](#)

Physics of Fluids **24**, 085104 (2012); <https://doi.org/10.1063/1.4744988>

**APL Machine Learning**

Open, quality research for the networking communities

**Now Open for Submissions**

LEARN MORE



# Large-scale structures of turbulent Rayleigh–Bénard convection in a slim-box

Cite as: Phys. Fluids **33**, 065103 (2021); doi: [10.1063/5.0048775](https://doi.org/10.1063/5.0048775)

Submitted: 26 February 2021 · Accepted: 13 April 2021 ·

Published Online: 1 June 2021



Wen-Feng Zhou (周文丰),<sup>1,2</sup> and Jun Chen (陈军)<sup>2,a)</sup>

## AFFILIATIONS

<sup>1</sup>Hypervelocity Aerodynamics Institute, China Aerodynamics Research and Development Centre, Mianyang 621000, China

<sup>2</sup>State Key Laboratory for Turbulence and Complex Systems, College of Engineering, Peking University, Beijing 100871, China

<sup>a)</sup>Author to whom correspondence should be addressed: [jun@pku.edu.cn](mailto:jun@pku.edu.cn). URL: [https://www.researchgate.net/profile/Jun\\_Chen21](https://www.researchgate.net/profile/Jun_Chen21)

## ABSTRACT

We report a numerical study of the large-scale structure of turbulent Rayleigh–Bénard convection (RBC) in a slim-box using direct numerical simulations. The simulations are performed in a rectangular cell of 1/6 depth-to-width ratio with the Rayleigh number from  $Ra = 1 \times 10^7$  to  $5 \times 10^9$  and Prandtl number equal to 0.7. It turns out that the large-scale circulation is driven by the jet flows, which consist of thermal plume clusters emitted from the conducting plate. The oblique impinging jet presents similar behavior for  $Ra$ . Moreover, the Reynolds number defined by the jet speed is approximated as a power law  $Re_m \sim Ra^{0.50}$ . The oblique jet impinges onto the horizontal plate and develops into a wall jet. The similar flow patterns over the plate indicate the coherent motion of the wall jet. The wall jet presents a three-layer structure including the viscous sublayer, the mixing layer, and the bulk. The velocity in each layer has its characteristic parameters. We analyzed the turbulent kinetic energy and dissipation and obtained the scaling laws of the horizontal and vertical velocity fluctuations and the heights of their peaks. The thermal boundary layer and the heat transfer on the plate are investigated. The self-similarity of the thermal boundary layer solution is verified by boundary layer theory. Further analysis reveals that the Nusselt number on the conducting plate is possessed by an exponential law of the horizontal location,  $Nu_x = Nu_m \exp(-\tilde{x})$ , where  $Nu_m$  is the maximum Nusselt number on the plate and  $\tilde{x}$  is the normalized horizontal distance to the stagnation point. We derived a power law of the maximum heat transfer on the plate by scaling analysis,  $Nu_m \sim Ra^{0.2925}$ , in agreement with the simulations. All results indicate that both the oblique impinging jet and the wall jet characterize the near-wall flow and the global heat transfer of turbulent RBC at moderate Rayleigh numbers.

© 2021 Author(s). All article content, except where otherwise noted, is licensed under a Creative Commons Attribution (CC BY) license (<http://creativecommons.org/licenses/by/4.0/>). <https://doi.org/10.1063/5.0048775>

## I. INTRODUCTION

Thermal convection plays an important role in many natural and engineering systems. Enormous phenomena in nature such as convection in the earth's mantle, cloud formation, and large-scale circulation (LSC) in the ocean are mainly driven by convection.<sup>1–6</sup> Of the many different forms of thermal convection, Rayleigh–Bénard convection (RBC) is by far the most studied. RBC occurs when a fluid in a confined area is heated from the bottom at high temperature and cooled from the top.<sup>7</sup> For a certain range of temperature differences, special features such as thermal plumes, LSC, and flow reversals have been observed.<sup>8–13</sup> Turbulent RBC is conventionally divided into a boundary layer (BL) and a bulk flow region.<sup>14,15</sup>

The heat transfer in a confined area filled with a fluid of width  $L_x$ , depth  $L_y$ , and height  $L_z$  is determined by a temperature difference  $\Delta T$ . The conditions are usually described by three dimensionless parameters, namely the Rayleigh number  $Ra = g\beta\Delta TL_z^3/(\nu\kappa)$ , the Prandtl

number  $Pr = \nu/\kappa$ , and the aspect ratio  $L_x/L_z$ . Here,  $g$  is the acceleration due to gravity,  $\beta$  the thermal expansion coefficient,  $\nu$  the kinematic viscosity, and  $\kappa$  the thermal diffusivity, respectively. Two global output parameters are dimensionless heat transfer  $Nu = q/(\kappa\Delta T/L_z)$  and flow intensity  $Re = UL/\nu$ , where  $q$  is heat flux and  $U$  and  $L$  are characteristic velocity and length, respectively, chosen appropriately for specific research. In order to control the flow and enhance the heat transfer for engineering purposes, huge efforts have been paid to distinguish the optimal boundary conditions and fluid properties by adopting the geometrical confinement,<sup>16–21</sup> adding roughness elements,<sup>22–24</sup> applying harmonic vibrations,<sup>25,26</sup> and inducing phase change.<sup>27</sup> Despite the simple configuration, many outstanding questions regarding the nature of turbulent RBC remain unanswered.

In a slim rectangular container of aspect ratio one ( $L_x/L_z = 1$ ) with relatively small depth ( $L_y/L_x = 1/6$ ), the flow is usually characterized by a dominant roll (also LSC) lying in the vertical square

section parallel to the front-end walls.<sup>10,28</sup> The LSC confined in between the walls may induce other large-scale structures. Those structures include the corner roll (CR),<sup>29</sup> the wind-shearing boundary layer and intensively ejecting plumes.<sup>10,30–32</sup> They jointly dominate heat transfer in an RB cell. The fluid driven by LSC and CR near the horizontal plate determines the local heat flux. It has been found that the local  $Nu$  (defined as  $Nu_x = -[(\partial T/\partial z)/(\Delta T/L_z)]_{z=0}$ ) reaches its maximum at the stagnation point and decays along the streamwise direction.<sup>10,33–35</sup> Additionally, thermal structures and the second peak of streamwise turbulent kinetic energy (TKE) are present in this region.<sup>10,36</sup> These phenomena are attributed to the flow between LSC and CR impinging on the plate. Additionally, the wall jet in RBC (RB-WJ) develops along the plate in the presence of the oblique jet impingement. These observations urge to pay more attention to the heat transfer induced by the jet.

The development of flow ejected by a nozzle parallel to an infinite plane is called the plane wall jet (PWJ) here, to distinguish it from the jet-like flow in the RBC. Both the oblique impinging jet (OIJ) and the PWJ have been studied for decades due to its enormous applications for engineering purpose. Goldstein and Franchett<sup>37</sup> found that the local  $Nu$  of the oblique plane jet exhibits a local maximum, along with an exponential decay. Narayan and Narasimha first suggested that the wall-bounded flow possesses a unique scaling law while being normalized with the momentum rate and the height of the outer region of PWJ.<sup>83</sup> The streamwise similarity of PWJ is characterized by the momentum rate  $M = \int_0^\infty U^2 dz$ , the maximum velocity at a given section  $U_m$ , the streamwise location  $x$ , and viscosity  $\nu$

$$\frac{U_m \nu}{M} \sim \left( \frac{xM}{\nu^2} \right)^{n_u}, \quad (1)$$

$$\frac{z_t M}{\nu^2} \sim \left( \frac{xM}{\nu^2} \right)^{n_z}, \quad (2)$$

where  $z_t$  is the height of the mean velocity equal to one half of the maximum velocity  $U_m$ . The normalized velocity in Eq. (1) and the height in Eq. (2) are the parameters of the jet flow expressed as the functions of streamwise position.

The scaling laws of the momentum rate have been asserted in a wide range of jets without heat transfer.<sup>38–41</sup> For the PWJ, the power exponent  $n_u = -1/2$  was first deduced by Glauert<sup>39</sup> by introducing similarity solution of plane laminar and turbulent wall jet (WJ) without wall stress. Myers *et al.*<sup>42</sup> and Gersten<sup>43</sup> also obtained  $n_u = -1/2$  with an integral method. By experimentally measuring  $n_{zt}$ , Gupta *et al.*<sup>41</sup> found the  $n_{zt}$  is close to 1.00, whereas Wagnanski *et al.*<sup>44</sup> suggested  $n_{zt} = 0.88$ , and Narasimha *et al.*<sup>40</sup> gave  $n_{zt} = 0.91$ . Launder<sup>45</sup> proposed that  $z_t$  demonstrates a linear growth with regard to the case of  $n_{zt} = 1.00$ . Besides the scaling law of the streamwise similarity, the TKE was investigated,<sup>46,47</sup> and twin peaks of the vertical TKE profile were found to be a feature of turbulent PWJ. The results showed that, when production is low, more energy would be transported to the region in between the two peaks. Fruitful knowledge of the turbulent PWJ flow is helpful for understanding the energy transportation of large-scale motions in RBC.

The PWJ is usually scaled by two reference heights and velocities corresponding to the inner and outer layers, but this scheme seems oversimplified for turbulent shear flows.<sup>48,49</sup> The turbulent boundary layer (TBL), for example, presents a multilayer structure as being,

respectively, dominated by its own balance in each layer. Recently, the wind-shearing and plume-ejecting of turbulent RBC have been investigated and described by the theory of structure ensemble dynamics (SED),<sup>10</sup> which provides a method to illuminate the multilayer structure of wall-bounded turbulent thermal convection.

In this paper, we investigate OIJ and WJ by analyzing the momentum and heat transfer in RBC. The present work is organized as follows. In Sec. II, we introduce the mathematical equations and numerical methods of simulating the turbulent Rayleigh–Bénard convection. The features of the impinging jet flow including the similarity of integration variables and local mean profiles of WJ are discussed in Sec. III. The energy flux carried by the OIJ and the scaling of heat transfer on the plate are presented in Sec. IV. Finally, the summary is given in Sec. V.

## II. COMPUTATIONAL SETUP

Direct numerical simulation (DNS) of turbulent Rayleigh–Bénard convection has been performed using a second-order finite-difference code in a slim-box domain as described in detail by Verzicco and Orlandi<sup>50</sup> and Verzicco and Camussi.<sup>51</sup> The dimensionless conservation laws of momentum, energy, and mass in the Oberbeck–Boussinesq approximation with gravitational acceleration in the  $z$ -direction read

$$\frac{\partial \mathbf{u}}{\partial t} + (\mathbf{u} \cdot \nabla) \mathbf{u} = -\nabla p + \theta \mathbf{e}_z + \sqrt{\frac{Pr}{Ra}} \nabla^2 \mathbf{u}, \quad (3)$$

$$\frac{\partial \theta}{\partial t} + (\mathbf{u} \cdot \nabla) \theta = \sqrt{\frac{1}{PrRa}} \nabla^2 \theta, \quad (4)$$

$$\nabla \cdot \mathbf{u} = 0. \quad (5)$$

Here  $\mathbf{u}$ ,  $\theta$ ,  $p$ , and  $\mathbf{e}_z$  denote the dimensionless velocity, temperature, dynamic pressure, and unit vector in  $z$ -direction, respectively. We have performed DNS in a slim-box of aspect ratio  $L_x : L_y : L_z = 1 : 1/6 : 1$ .

The boundary conditions are set to close the equations as follows. Fixed temperatures are set on top and bottom plates, and adiabatic condition on side-walls. Periodic boundary is applied in the depth direction and nonslip condition for all solid walls. The simulations are initialized by a fluid at rest and an even temperature. The box height  $L_z$  and the free fall velocity  $U_f = (\beta L_z g \Delta T)^{1/2}$  are used as references for distance and velocity, and the temperature is normalized by  $\theta = (T - T_c)/\Delta T$ , where  $\Delta T$  denotes the difference between the temperatures of the top and bottom plates and  $T_c$  is their mean value. Therefore, the  $Pr$  number  $Pr = \nu/\kappa$  and the aspect ratio present as the parameters fixing the set of equations. The variables are normalized using the free fall velocity  $U_f = \sqrt{RaPr}(\kappa/L_z)$ , the pressure  $P_0 = RaPr(\rho\kappa^2)/L_z^2$ , and the timescale  $T_0 = (L_z^2/\kappa)\sqrt{RaPr}$ . These parameters are determined according to Zou *et al.*<sup>10</sup> to fulfill the resolution requirements for a DNS. The  $Ra$  number varies between  $1 \times 10^7$  and  $5 \times 10^9$ , while the  $Pr$  number is kept constant at  $Pr = 0.7$ .

Kolmogorov and Batchelor scales were resolved to ensure appropriate number of nodes. The globally averaged Kolmogorov length scale  $\eta_k$  was calculated by the relation  $\eta_k = Pr^{1/2}[Ra(Nu - 1)]^{-1/4}$ , and the Batchelor length scale  $\eta_{Ba}$  was estimated through  $\eta_{Ba} = \eta_k Pr^{-1/2}$ . Since the  $Pr$  number in the present work is less than unit, resolving Kolmogorov scale is necessary. The BL region requires finer spatial resolution than the bulk region to resolve the near-wall flow. Neglecting this might lead to unrealistic plumes, and thus,  $Nu$

**TABLE I.** Simulation parameters for  $Pr=0.7$ ,  $L_x : L_y : L_z = 1 : 1/6 : 1$ . The Reynolds number  $Re_m$  as defined in Eq. (7); the number of mesh nodes in the  $i$ -direction  $N_i$ ,  $i = x, y, z$ ; the number of nodes in the thermal/viscous BL as used in DNS; the Nusselt number  $Nu_j$ , where  $j = 1, 2, 3$  denote the  $Nu$ , respectively, defined by volume integration, momentum dissipation, and thermal dissipation; the Kolmogorov scale  $\eta_k$ ; the Batchelor scale  $\eta_{Ba}$ ; the mesh nodes for the viscous and thermal BL  $N_{u,bl}$ ,  $N_{\theta,bl}$ ; the number of dimensionless time units  $\tau$  used for averaging; and the minimum and maximum heights in  $z$ -direction  $\Delta_{min}$  and  $\Delta_{max}$ .

$Ra$	$Pr$	$Re_m$	$N_x \times N_y \times N_z$	$Nu_1$	$Nu_2$	$Nu_3$	$\Delta_{min}/L_z$	$\Delta_{max}/L_z$	$\eta_k/L_z$	$\eta_{Ba}/L_z$	$N_{u,bl}$	$N_{\theta,bl}$	$t_{avg}/t_f$
$1 \times 10^7$	0.7	715	$768 \times 128 \times 512$	18.2	18.2	18.2	$0.23 \times 10^{-3}$	$4.2 \times 10^{-3}$	$7.30 \times 10^{-3}$	$8.73 \times 10^{-3}$	$72 > 4$	$52 > 4$	480
$5 \times 10^7$	0.7	1500	$768 \times 128 \times 512$	29.1	29.1	29.0	$0.23 \times 10^{-3}$	$4.2 \times 10^{-3}$	$4.32 \times 10^{-3}$	$5.16 \times 10^{-3}$	$53 > 4$	$71 > 5$	320
$1 \times 10^8$	0.7	2069	$768 \times 128 \times 512$	34.7	34.2	34.3	$0.23 \times 10^{-3}$	$4.2 \times 10^{-3}$	$3.47 \times 10^{-3}$	$4.15 \times 10^{-3}$	$72 > 5$	$29 > 5$	300
$5 \times 10^8$	0.7	4446	$768 \times 128 \times 512$	55.8	54.8	55.3	$0.23 \times 10^{-3}$	$4.2 \times 10^{-3}$	$2.06 \times 10^{-3}$	$2.46 \times 10^{-3}$	$62 > 6$	$19 > 7$	400
$1 \times 10^9$	0.7	5189	$1024 \times 128 \times 800$	68.9	69.3	68.5	$0.08 \times 10^{-3}$	$1.8 \times 10^{-3}$	$1.64 \times 10^{-3}$	$1.96 \times 10^{-3}$	$83 > 7$	$38 > 7$	300
$5 \times 10^9$	0.7	13862	$1024 \times 128 \times 800$	110.8	109.1	109.7	$0.10 \times 10^{-3}$	$1.8 \times 10^{-3}$	$0.97 \times 10^{-3}$	$1.16 \times 10^{-3}$	$86 > 8$	$22 > 9$	400

will be higher than the real solution.<sup>52</sup> The essential number of nodes in the BL has been estimated in the simulations of Zhou and Chen<sup>29</sup> and displayed in Table I. The spatially averaged Kolmogorov scale is used as the required resolution for the bulk region in each direction. In order to examine the  $Nu$  number, we compared three types of  $Nu$ , which are listed in Table I. They are the spatiotemporal average of the heat flux in the box  $Nu_1 = 1 + \sqrt{RaPr} \langle w\theta \rangle_{V,t}$ , the heat flux of global thermal dissipation  $Nu_2 = \langle |\nabla\theta|^2 \rangle_{V,t}$ , and the global momentum dissipation  $Nu_3 = 1 + Pr \langle |\nabla\mathbf{u}|^2 \rangle_{V,t}$ . The  $N_{u,bl}$  and  $N_{\theta,bl}$  are the least number of grid nodes required inside the viscous/thermal BL estimated by Shishkina *et al.*<sup>53</sup> The simulated data<sup>29</sup> showed that the  $Ra$  dependence of the geometry of flow structures is obvious. The size of flow structures usually decreases with increasing  $Ra$ .

### III. SIMILARITY OF THE JET IN RB CELL

#### A. The oblique impinging jet and its Reynolds number scaling

Figure 1(a) presents the speed field, that is, the magnitude of time-averaged velocity,  $U_s(x, z) = \sqrt{U^2 + W^2}$ . All data presented below have been averaged in the depth ( $y$ ) direction. The downwelling stream, called the “ejecting stream” near the left sidewall, is deflected by the CR and leads to an oblique jet impinging on the horizontal plate. Therefore, the motion of LSC in combination with the CR forms an OIJ analogous to the OIJ impinging on an infinite plane<sup>37</sup> along with a PWJ.<sup>40,41,43,48</sup> Note that this scenario occurs at the diagonal (down-left/up-right) corners of the RB cell.

The speed profiles normal to the slip line at five locations named *loc1* to *loc5* [as marked in Fig. 1(a)] are plotted together in Fig. 1(b). The line at *loc3* connects the centers of the CR and LSC. Other lines of speed profiles are parallel to this line. The inclination angle between the line and the bottom plate is called  $\theta_0$ . The speed profiles present a parabolic function. The similarity of the profiles along the stagnation streamline indicates that the fluid motion along the stagnation streamline sustains a free-jet-like flow between CR and LSC. Moreover, the deviation of the profile at *loc5* is caused by the stagnation of the jet on the bottom plate.

To investigate the effect of  $Ra$ , the speed profiles at *loc3* for different  $Ras$  are scaled by the correspondent maxima, and the length scales are scaled by the distance between LSC and CR

$$\tilde{U}_j = \frac{U_s}{U_{\max}} \quad \text{and} \quad \tilde{L} = \frac{L_{cr}}{L_{lc}}, \quad (6)$$

where the size of CR  $L_{cr}$  is the distance to the center of CR on *loc3*,  $L_{lc} = \sqrt{(x_{lsc} - x_{cr})^2 + (z_{lsc} - z_{cr})^2}$ ,  $(x_{lsc}, z_{lsc})$ , and  $(x_{cr}, z_{cr})$  are the coordinates of the centers of LSC and CR, respectively. Figure 2(a) shows a similarity of OIJ speed profile for different  $Ras$ , which can be empirically described in form of beta function  $\tilde{U}_j = 4.0\tilde{L}^{0.80}(1 - \tilde{L})^{1.30}$ . The slip line is laid at  $\tilde{L} = 0.126$ , closer to CR than LSC, indicating that the OIJ contributes more energy to LSC than CR.

The similarity of the speed profiles of  $U_s$  indicates that the normalized jet speed  $U_{\max}$  and  $L_{lc}$  can be used as the parameters to scale the OIJ speed profile. Figure 2(b) shows  $Re_m$ , and the Reynolds number defined by the above two parameters in combination with viscosity  $\nu$  fulfills an  $Ra$  power law

$$Re_m \equiv \frac{U_{\max} L_{lc}}{\nu} = 0.20 Ra^{0.50}. \quad (7)$$

The scaling is consistent with the previous scaling of the Reynolds number defined by large-scale motion.<sup>54–56</sup> The Reynolds number defined by the velocity of LSC in the RBC (also called the most probable velocity in Ref. 56) has the same scaling,  $Re \sim Ra^{0.50}$ . The coincidence of the scalings indicates that the OIJ is the large-scale structure driving the motions of LSC and CR.

#### B. Similarity of RB-WJ

The fluid of OIJ convecting along the shear layer between LSC and CR eventually impinges onto the horizontal plate. Since the impingement causes an intensive pressure gradient near the stagnation point, the WJ flow on the plate no longer conforms to the conventional theory of zero pressure gradient TBL. We here apply the knowledge of PWJ to describe the velocity and heat transfer of the WJ in turbulent RB system.

Kinematic momentum rate  $M = U^2 L$  is often used as a scale for the PWJ and the boundary layer.<sup>41,43,48,57</sup> Two definitions of the momentum rate are usually used to scale WJs.<sup>40</sup> They are the nozzle momentum rate  $M_{noz} = U_{noz}^2 b$  and the local momentum rate  $M(x) = \int_0^L U_j^2(x, z) dz$ , where  $U_j$  is the nozzle exit velocity and  $b$  is the nozzle height,  $U_j(x, z)$  is the local velocity of the jet flow, and  $L$  is a reference height.

If the WJ is independent of the initial conditions of the nozzle, the flow would be scaled by local momentum rate  $M(x)$ , allowing for self-similar development with regard to the local conditions.<sup>41</sup> Since



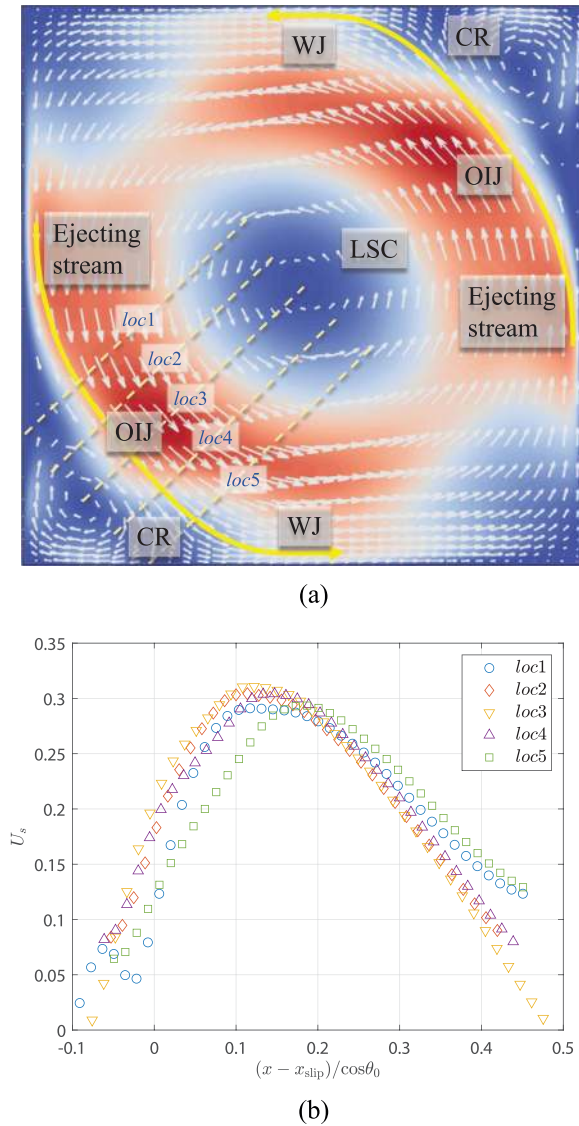


**FIG. 1.** Spatial distribution of the mean speed at  $Ra = 1 \times 10^8$ : (a) the time-averaged speed on  $xz$ -plane. Blue denotes low speed, and red denotes high speed. (b) Speed profiles on the five lines normal to the slip line, and  $x_{slip}$  is the abscissa of slip line.

the convection flow in response to RB-OIJ does not have a definite initial condition like the flow being ejected from a nozzle, the local momentum rate  $M(x)$  is then employed to scale WJ here.

The RB-WJ consists of two flow regions—the near-wall region and the bulk region, as schematically shown in Fig. 3. The flow in the near-wall region is intensively confined by the plate and dominated by viscosity. The near-wall region includes the viscous sublayer and the mixing layer. The bulk region, on the other hand, is dominated by inertia. The mixing layer is formed by the interaction between the viscosity of the sublayer and the inertia of the bulk. The characteristic velocity and the height of the bulk are the maximum velocity  $U_{m,b}$  and

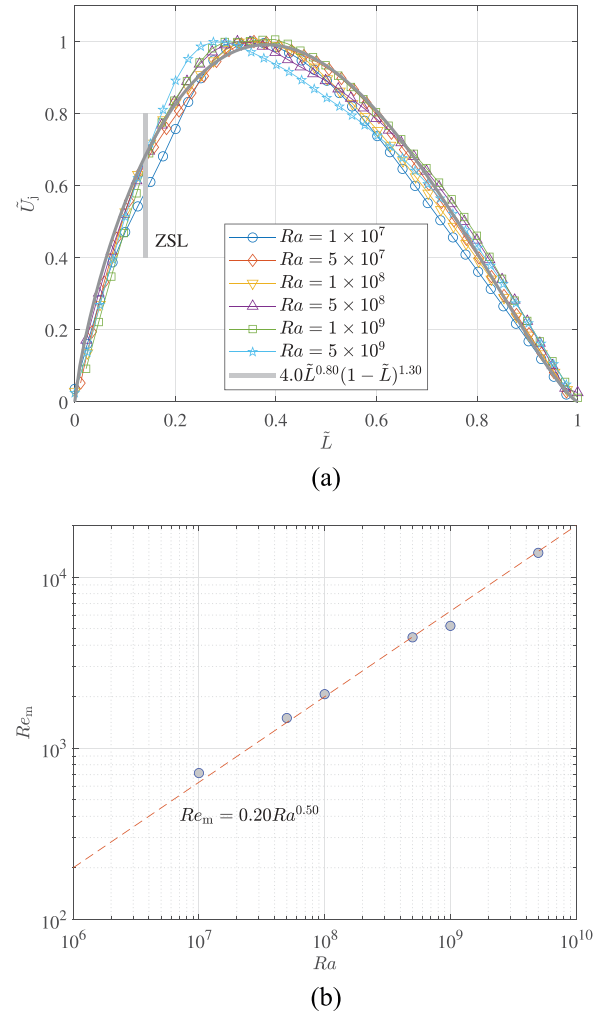


**FIG. 2.** The normalized speed of OIJ and the Reynolds number defined by it: (a) the speed profiles of OIJ  $\tilde{U}_i$  on the line connecting the cores of LSC and CR with  $Ra$  from  $1 \times 10^7$  to  $5 \times 10^9$  and (b) the Reynolds number of OIJ  $Re_m$  as a power function of  $Ra$ .

half-height  $z_{t,b}$ , where the mean velocity is equal to  $U_{m,b}/2$ , respectively.<sup>40</sup> The inner peak velocity  $U_{m,w}$  and the corresponding height  $z_{t,w}$  are the characteristic scales for the near-wall region. For the viscous sublayer, the flow is dominated by the law of wall and correspondingly scaled by the friction velocity  $u_\tau = \sqrt{(\nu \frac{\partial U}{\partial z})_{z=0}}$  along with the viscous scale  $\nu/u_\tau$ .

The inner peak velocity in the near-wall region  $U_{m,w}$  along the bottom plate (the direction of  $x$ ) is shown in Fig. 4(a), which takes with the  $Ra$  of  $1 \times 10^7$  to  $5 \times 10^9$  over a range of the distance to the left sidewall,  $x = 0.40$ – $0.60$ . To eliminate the geometrical and bulk flow effects, the distance to the stagnation point is used as the horizontal distance,  $\Delta x = x - x_a$ , where  $x_a$  is the horizontal distance of the stagnation point to the left sidewall. Here, both  $U_{m,w}$  and  $\Delta x$  are scaled with the local momentum rate  $M_w(x) = \int_0^{z_{min}} U^2(x, z) dz$  (per unit width) and viscosity  $\nu$ , where  $z_{min}$  is the height of the minimum

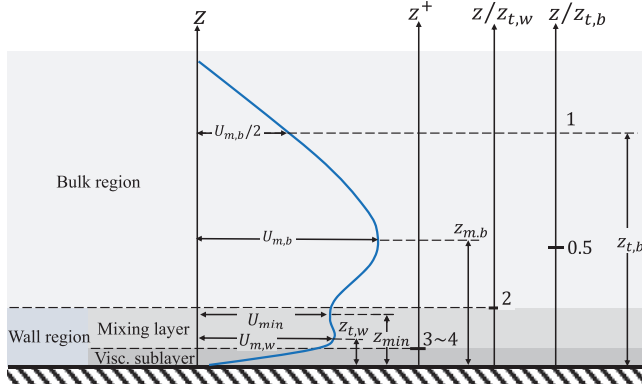


**FIG. 3.** Schematic plot of the velocity profile of turbulent RBC including the viscous sublayer, the mixing layer and the bulk region. The thickness of each layer is determined by corresponding normalized height— $z^+ = 3\sim 4$  for the viscous sublayer,  $z/z_{t,w} = 2$ , for the mixing layer, and  $z/z_{t,b} = 0.5$  for the bulk region, as discussed in Sec. III D.

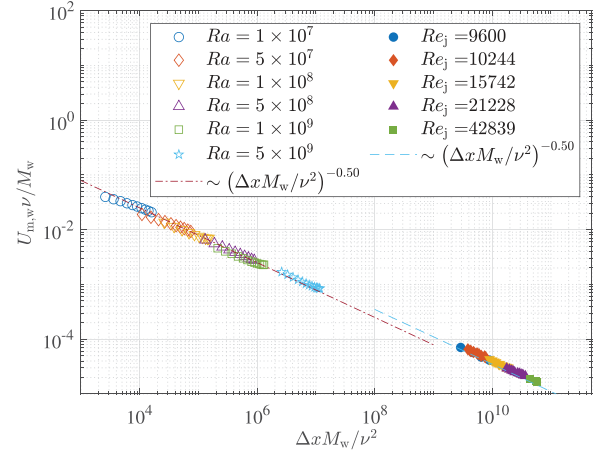
velocity in between two velocity peaks,  $U_{m,b}$  and  $U_{m,w}$  (see Fig. 3). For the “single peak” of velocity,  $z_{min}$  is set to equal  $2z_{t,w}$ . Figure 4(a) shows that the normalized maximum velocity  $U_{m,w}\nu/M_w$  varying as a power function of  $\Delta x M_w/\nu^2$  with an exponent of  $n_u = -0.50$

$$\frac{U_{m,w}\nu}{M_w} = A_u \left( \frac{\Delta x M_w}{\nu^2} \right)^{n_u}, \quad (8)$$

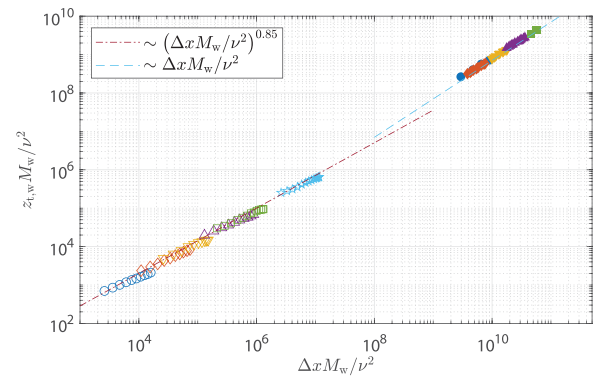
where  $A_u = 2.4$  for all  $Ra$  numbers of the present study. The results of turbulent PWJs are also presented in Fig. 4(a) for comparison, and their power exponent and the factor are correspondingly  $n_u = -0.50$  and  $A_u = 4.1$ . Equation (8) can be rewritten as  $M_w = \int_0^h U^2 dz = U_{m,w}^2 \Delta x / A_u^2$  for  $n_u = -0.50$ . Considering the different outer regions of the two systems, the integration scales for the near-wall region are taken as  $h = z_{min}$  for the RBC and  $h = \infty$  for the PWJ, respectively.

The magnitudes of  $(n_u, A_u)$  for turbulent PWJ have been extensively studied in the literature. Schwarz and Cosart suggested  $(-0.555, 5.395)$ ,<sup>58</sup> Narasimha *et al.*  $(-0.506, 4.6)$ ,<sup>40</sup> and Wynanski *et al.*  $(-0.472, 1.473)$ .<sup>44</sup> Note that the above parameter sets of  $(n_u, A_u)$  were scaled with  $M_j$  rather than  $M(x)$ . As for the difference of  $M_{noz}$  and  $M(x)$ , Narasimha *et al.* claimed that the correlation is the same either for  $M_j$  or  $M(x)$ ,<sup>40</sup> whereas Gupta *et al.* suggested that the local  $M(x)$  is a better scale for the PWJ.<sup>41</sup> As shown in Fig. 4, the unique power exponent of the maximum velocity while being scaled by  $M(x)-\nu$  indicates the same behavior of the near-wall flows for the PWJ and the RB-WJ.

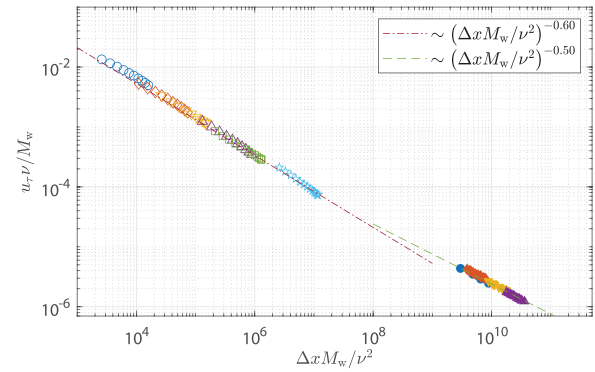
It is noteworthy that  $\Delta x M_w/\nu^2$  of PWJ is several order of magnitude greater than that of RB-WJ. In order to understand the derivation of the two systems, we take the nozzle height  $b$  as an extra parameter in the WJ flow and will get three dimensionless independent variables  $\Pi_1 = z/b$ ,  $\Pi_2 = x/b$ , and  $\Pi_3 = \sqrt{M_j b}/\nu^2$ . The nozzle height  $b$  as estimated by the half width of speed profile of OIJ  $b = L_c/2$  along with the maximum velocity of the OIJ leads to  $Re_j$  for the RBC on the order of  $10^2$  to  $10^3$ . On the other hand,  $Re_j$  for PWJ is usually on the order of  $10^3$  to  $10^4$ . The Reynolds numbers of the two systems are close. Considering the fact that the RB-WJ is driven by circulation of the thermal plumes rather than by momentum fluid from a nozzle, the absence of an exit of fluid makes it hard to accurately determine  $b$  for



(a)



(b)



(c)

**FIG. 4.** The scalings of the normalized (a)  $U_{m,w}$ , (b)  $z_{t,w}$ , and (c)  $u_c$  against the normalized  $x$ . The data are obtained from the experiments of Schwarz *et al.*<sup>58</sup>  $Re_j = 42\,839$ , Eriksson *et al.*<sup>59</sup>  $Re_j = 9600$ , and Gupta *et al.*<sup>41</sup>  $Re_j = 10\,244$ ,  $15\,742$ , and  $21\,228$ , where  $Re_j = U_j b/\nu$ ,  $U_j$  is the nozzle exit velocity, and  $b$  is the nozzle height.

RBC. The flow state in the near-wall region in RBC indicates the similar behavior of the two systems. Then, the magnitude of  $\sqrt{M_j b}/\nu^2$  can be measured by the nozzle exit Reynolds number  $Re_j$ . The estimated  $b/L_z$  for RBC is about 0.3, and the maximum of  $x/b$  is about 3.

On the other hand,  $x/b$  for the PWJ (presented in Fig. 4) is usually on the order of  $10^3$ . Considering  $\Delta x M_w / \nu^2 = \Pi_2 \Pi_3^2$ , one then obtains that the normalized  $\Delta x$  is on the order of  $10^4$  to  $10^6$  for RBC, and  $10^9$  to  $10^{11}$  for PWJ. This fact is consistent with the results in Fig. 4. The data of the two systems collapse well with a similar scaling law that strongly implies the similarity of the scales, which are independent of the nozzle exit Reynolds number  $Re_j$  and the nozzle height  $b$ .

The thickness of the near-wall region  $z_{t,w}$  scaled by  $M_w - \nu$ , as shown in Fig. 4(b), has a scaling law

$$\frac{z_{t,w} M_w}{\nu^2} = A_{zt} \left( \frac{\Delta x M_w}{\nu^2} \right)^{n_{zt}}, \quad (9)$$

where  $A_{zt} = 0.73$  and  $n_{zt} = 0.85$  for the simulated RB system. Here, the near-wall region thickness  $z_{t,w}$  is defined as the height of the maximum velocity in the inner layer, corresponding to the half-height of the PWJ. As George *et al.* pointed out, the maximum velocity height and the half-height have the similar behavior along the streamwise direction,<sup>48</sup> but the half-height is more stable for experimental results of the PWJ.<sup>41</sup> Narasimha *et al.*<sup>40</sup> also found that the ratio of half-height to the maximum velocity height is about 6.2, independent of  $\Delta x M_w / \nu^2$ . Hence, the two scales are comparable.

The thickness of the near-wall flow of the PWJ has been extensively investigated. George *et al.* suggested that  $n_{zt} = 0.915$  by semi-empirical analysis (normalized by  $M_j - \nu$ ) and also derived that the streamwise gradient of  $z_{t,w}$ ,  $dz_{t,w}/dx$  is proportional to the shear stress.<sup>48</sup> For asymptotic condition,  $dz_{t,w}/dx \rightarrow 0$ ,  $n_{zt,w}$  is less than unit. Here, one can see that the flow in RBC satisfies the scenario of George *et al.*, but the power exponent is less than that in the WJ.<sup>40,48,49</sup> This indicates that the turbulence is suppressed by the downward flow of LSC in vertical direction, and therefore, the growth of wall-bounded turbulence of RBC is weaker than that in turbulent PWJ.

Two Reynolds numbers,  $Re_{M_x}$  and  $Re_{M_z}$ , are defined by the normalized physical parameters,  $U_{m,w} \nu / M_w$ ,  $\Delta x M_w / \nu^2$ , and  $z_{t,w} M_w / \nu^2$ , to characterize streamwise and vertical development of the near-wall flow, respectively. The streamwise  $Re$  number  $Re_{M_x} = \sqrt{\Delta x M_w} / \nu$  and vertical  $Re$  number  $Re_{M_z} = U_{m,w} z_{t,w} / \nu$ . The correlation of  $Re_{M_x}$  and  $Re_{M_z}$  is obtained by combining Eqs. (8) and (9):  $Re_{M_z} = \frac{U_{m,w} z_{t,w}}{\nu} = (U_{m,w} \nu / M_w) (z_{t,w} M_w / \nu^2) = A_u A_{zt} Re_{M_x}^{2(n_{zt} + n_u)} \sim Re_{M_x}^{0.70}$ . Thus,  $Re_{M_x} \approx 2300$  and  $Re_{M_z} \approx 360$  for  $Ra = 5 \times 10^9$  at  $x = 0.5$ .

The friction velocity  $u_\tau$  scaled by  $M_w - \nu$  is shown in Fig. 4(c), and its scaling is shown as follows:

$$\frac{u_\tau \nu}{M_w} = A_{u_\tau} \left( \frac{\Delta x M_w}{\nu^2} \right)^{n_{u_\tau}}, \quad (10)$$

where  $A_{u_\tau} = 1.40$  and  $n_{u_\tau} = -0.60$  for the present RBC. The turbulent PWJ gives  $A_{u_\tau} = 0.25$  and  $n_{u_\tau} = -0.50$ . In comparison, Wygnanski *et al.* suggested  $A_{u_\tau} = 0.382$  and  $n_{u_\tau} = -0.535$  as scaled by  $M_j - \nu$  in turbulent PWJ.<sup>44</sup>

The results of turbulent PWJ show that  $u_\tau / U_{m,w}$  weakly depends on  $\frac{x M_w}{\nu^2}$ . George *et al.*<sup>48</sup> suggested  $u_\tau / U_{m,w} = 0.023 (z_T^+)^{-0.0362} \times \exp \left( \frac{2.9}{(\ln z_T^+)^{0.46}} \right)$ , where  $z_T^+ = z_T u_\tau / \nu = \frac{z_T M_w u_\tau \nu}{M_w} \sim \left( \frac{x M_w}{\nu^2} \right)^{0.25}$ . In the present study, combining Eq. (8) with (10) and taking the power exponents of the RBC, we have  $u_\tau / U_{m,w} \sim \left( \frac{x M_w}{\nu^2} \right)^{-0.10}$ . It is seen that the

impingement angle and confinement of the RB cell have finite influence on the similarity of the near-wall flow of RB system.

### C. Correlation of scalings

The scaling of  $U_{m,w}$  in RBC agrees well with the turbulent WJ as seen in Fig. 4. The scalings of  $z_{t,w}$  and  $u_\tau$  show that the LSC and the confinement of the flow have finite effects on the near-wall flow. The correlation can be formularized by the horizontal equation of Eq. (3)<sup>48,60</sup>

$$\frac{\partial U^2}{\partial x} + \frac{\partial UW}{\partial z} = \frac{\partial}{\partial z} \left[ \nu \frac{\partial U}{\partial z} - \overline{u'w'} \right] - \frac{\partial}{\partial x} [\overline{u'u'} - \overline{w'w'}]. \quad (11)$$

Equation (11) has eliminated the pressure by integrating the vertical momentum equation of Eq. (3) and ignored the vertical integration of  $\frac{\partial \theta}{\partial x}$ . By integrating in  $z$  direction and considering the boundary conditions of wall, we obtain

$$\begin{aligned} \frac{d}{dx} \int_0^{z_0} U^2 + \overline{u'u'} - \overline{w'w'} dz + \frac{dz_0}{dx} [U^2 + \overline{u'u'} - \overline{w'w'}]_{z_0} + UW|_{z_0} \\ = -u_\tau^2 + \nu \frac{\partial U}{\partial z} \Big|_{z_0} - \overline{u'w'}|_{z_0}, \end{aligned} \quad (12)$$

where  $z_0$  is an appropriate height, corresponding to the infinite height in PWJ. As mentioned before, we have  $z_0 = z_{\min}$ , which means a position far away from the wall but not reaching out into the bulk. Finally, we have

$$UW|_{z_0} \approx 0, \quad \nu \frac{\partial U}{\partial z} \Big|_{z_0} \approx 0, \quad \overline{u'w'}|_{z_0} \approx 0, \quad \frac{dz_0}{dx} \approx 0 \quad (13)$$

and

$$\frac{d}{dx} \int_0^{z_0} U^2 + \overline{u'u'} - \overline{w'w'} dz = -u_\tau^2. \quad (14)$$

Since  $U^2 \gg \overline{u'u'} - \overline{w'w'}$ , Eq. (14) is as follows:

$$\frac{dM_w}{dx} = \frac{d}{dx} \int_0^{z_0} U^2 dz = -u_\tau^2. \quad (15)$$

Equation (15) is similar to result of Ref. 48. It demonstrates that the wall friction is attributed to the momentum loss.

A nondimensional momentum rate  $k_m$  is obtained when  $M_w$  is scaled by  $U_{\max}^2 z_T$

$$k_m = \frac{M_w}{U_{\max}^2 z_T}. \quad (16)$$

Wygnanski *et al.*<sup>44</sup> suggested  $k_m = 4.93$  for turbulent WJ.<sup>61</sup> The normalized momentum rate  $k_m$  varies in  $x$  direction with different  $Ras$  as seen in Fig. 5. With  $x$  and  $Ra$  increasing,  $k_m$  slowly grows till saturated, indicating an incomplete similarity. Similar behavior in PWJ is referred to Ref. 62. Renormalizing  $k_m$  with its value at  $x = x_a + 0.25$  gives that  $k_m / k_{m,s}$  is in range of 0.8–1.2. The study in turbulent PWJ by Wygnanski *et al.*<sup>44</sup> suggested that with increasing  $Ra$ ,  $k_m$  reaches a constant for  $Ra > 5.8 \times 10^{12}$ . In contrast,  $k_m$  at the location  $x = x_a + 0.25$  fulfills a power law  $k_m = 0.145 Ra^{0.12}$  (see the inset of Fig. 5). The finite  $Re$  effect on the flow is considerable at moderate  $Ra$ .

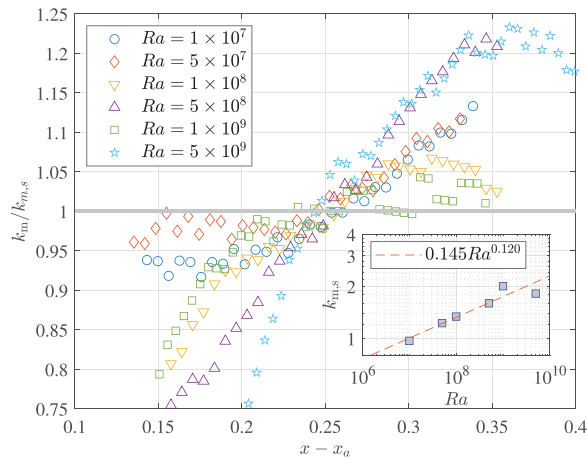


**FIG. 5.** The renormalized momentum rate  $k_m/k_{m,s}$  against  $x$ . The value of  $k_{m,s}$  is  $k_m$  at  $x = x_a + 0.25$ . The inset is the  $Ra$  dependence of  $k_{m,s}$ .

With Eq. (16), Eq. (15) can be rewritten as

$$\frac{dk_m U_{\max}^2 z_T}{dx} = -u_\tau^2. \quad (17)$$

Thus, by ignoring small variation of  $k_m$  the power exponents,  $n_{u_\tau}$ ,  $n_{z_t}$  and  $n_{u_\tau}$ , follow a relation as

$$2n_u + n_{z_t} - 1 = 2n_{u_\tau}. \quad (18)$$

With this equation, we have  $n_{u_\tau} = -0.575$  consistent with DNS result. The correlation of power exponents  $n_{u_\tau}$ ,  $n_{z_t}$ , and  $n_{u_\tau}$  reflects the fact that RB-WJ is featured by developing PWJ, but distinct from well-developed and wall-bounded turbulence.

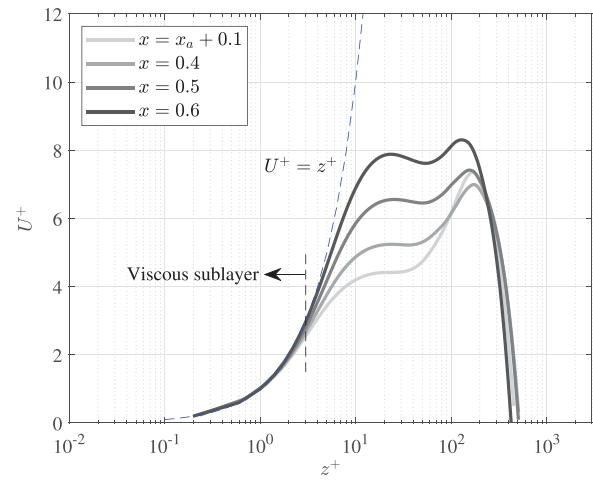
#### D. Multilayer structure of velocity profiles

The velocity profiles of RBC are compared with those of turbulent PWJ. The mean velocity profile normal to the plate is schematically shown in Fig. 3, which includes three layers. They can be scaled by the inner scale, the mixing layer scale, and the bulk scale, respectively.

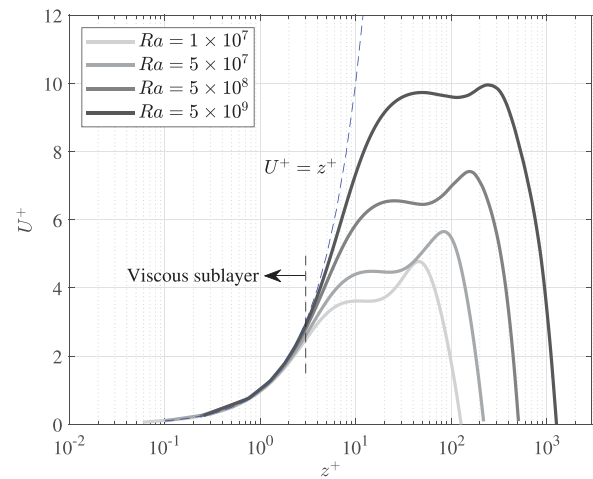
Figure 6 shows the vertical velocity profiles at various horizontal locations and  $Ra$ s being scaled by the friction velocity  $u_\tau$  and viscous scale  $\nu/u_\tau$ , that is,  $U^+ = U/u_\tau$  and  $z^+ = zu_\tau/\nu$ . The linear viscous sublayer conforms to the law of wall,  $U^+ = z^+$ . The thickness of the sublayer is about  $z^+ = 3-4$  in agreement with the measurements of a two-dimensional PWJ.<sup>59,63</sup> Note that this sublayer is thinner than that in TBL, which is about five to 10 wall units.<sup>64</sup> The different thicknesses are attributed to finite  $Re$  effect under the influence of buoyancy and pressure gradient.

The TBL at a relatively high Reynolds number with zero pressure gradient yields a well-developed viscous sublayer. However, the  $Re$  number of simulated RBCs is on the order of hundreds as estimated by  $Re_{Mz}$ . The small  $Re$  suppresses the momentum transport in the near-wall region and reduces the sublayer thickness. It is noted that with increasing  $Ra$ , the  $Re$  number increases, and the thickness of the sublayer increases thereafter [see Fig. 6(b)]. Moreover, the linearity region may reach up to the viscous sublayer of TBL at high  $Ra$ .

The mixing layer is scaled by  $U_{m,w}$ , and the height is scaled by  $z_{t,w}$  as shown in Fig. 7 in the range of  $0.6 < z/z_{t,w} < 2$  within the WJ



(a)



(b)

**FIG. 6.** The velocity profiles scaled by the inner velocity and length as a function of the height at (a)  $x = x_a + 0.1, 0.4, 0.5, 0.6$  with  $Ra = 5 \times 10^8$ , and (b)  $Ra = 1 \times 10^7, 5 \times 10^7, 5 \times 10^8, 5 \times 10^9$  at  $x = 0.5$ .

region and the simulated  $Ra$ s. In the mixing layer, the effect of momentum diffusion is remarkable, while the pressure gradient, the Reynolds stress, and the mean advection jointly dominate the flow. This region can be considered as the overlap region of turbulent PWJ,<sup>41,43,48</sup> which is laid below the maximum velocity. The  $Re_\tau$  dependence of the mixing layer can be expressed as the log-law<sup>43</sup> or the power law.<sup>41</sup> However, it has a larger extent in RBC, and its velocity profile is quite flat. Note that the flow further away from the plate no longer sustains its similarity due to the circulation of the bulk.

The turbulent PWJ is usually characterized by the momentum diffusion below  $z_{m,b}$ , and the outer region is filled with static fluid. In contrast, the region at the center of an RB cell is characterized by LSC. Velocity is scaled by  $U_{m,b}$ , and the height is scaled by  $z_{t,b}$  for this region. The velocity profiles are shown in Fig. 8. The normalized velocity at different horizontal locations in the range of  $z > 0.50z_{t,b}$  has the



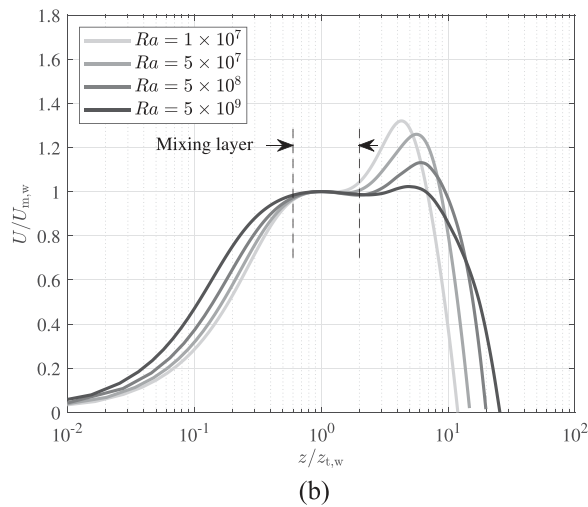
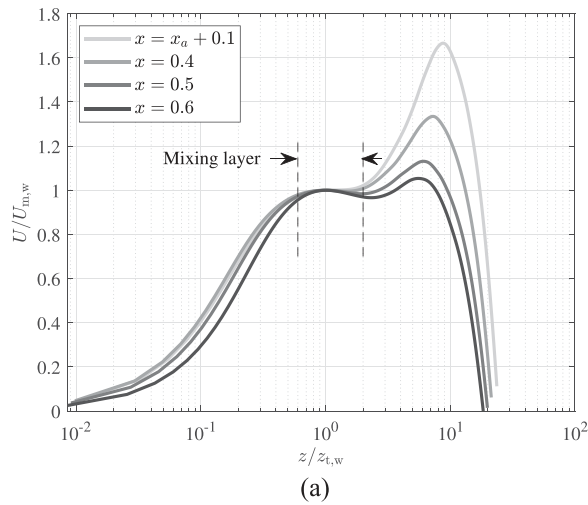


**FIG. 7.** The velocity profiles in scaled by the intermediate velocity and length as a function of height at (a)  $x = x_a + 0.1, 0.4, 0.5, 0.6$  with  $Ra = 5 \times 10^8$  and (b)  $Ra = 1 \times 10^7, 5 \times 10^7, 5 \times 10^8, 5 \times 10^9$  at  $x = 0.5$ .

same behavior at all simulated  $Ra$ s as it in the range of  $z > 0.1z_{t,b}$  for turbulent PWJ.<sup>41</sup> The geometry of the cell produces the circulation at the center. Therefore, the different outer flows of the two systems lead to different spatial ranges of similarity.

It is noted that the edge of the outer region, that is,  $x = 0.5$  [see Fig. 8(a)], is not a universal scale. It cannot be used as the characteristic height,  $z_{t,b}$ , as presented in Fig. 8(b). The reason is that for a larger  $Ra$ , the LSC becomes larger and stronger, and the bulk region owns a larger volume. Moreover, based on the rotation essence, the symmetry center should lay at the center of LSC rather than the wall.

### E. Similarity of the fluctuations in the near-wall region

The horizontal velocity fluctuation of RB-WJ  $\sigma_u^+ = \sqrt{u'^2}^+$  is calculated in comparison with that of turbulent PWJ. Figure 9 is the root mean square (rms) of the horizontal velocity  $\sigma_u^+$  at various horizontal

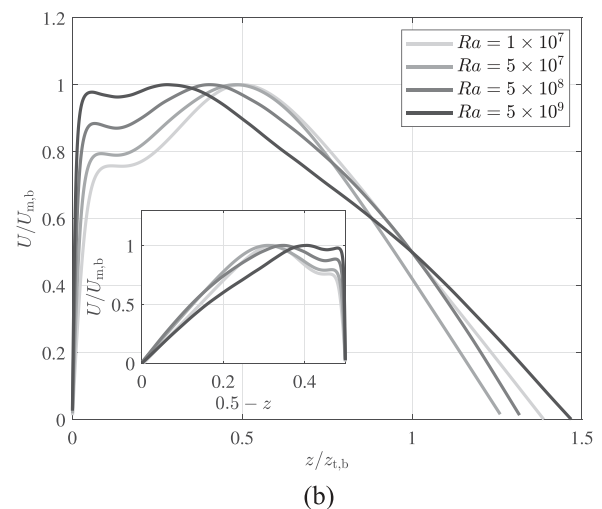
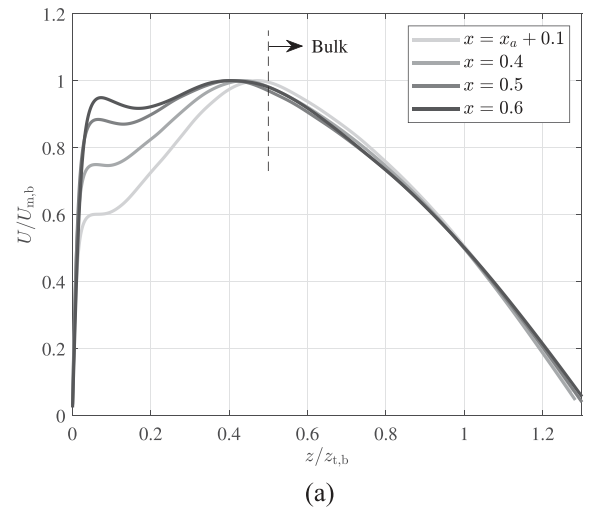


**FIG. 8.** The velocity profiles normalized by the outer velocity and length as a function of height at (a)  $x = x_a + 0.1, 0.4, 0.5, 0.6$  at  $Ra = 5 \times 10^8$  and (b)  $Ra = 1 \times 10^7, 5 \times 10^7, 5 \times 10^8, 5 \times 10^9$  at  $x = 0.5$ .

locations and  $Ra$ s. It shows that  $\sigma_u^+$  grows rapidly in the near-wall region ( $z^+ < 10$ ) and reaches the first peak at  $z_{\sigma_u, m1}^+$  (below  $z_{t,w}$ ), reminiscent of the results of turbulent PWJ.<sup>46</sup> The second peak appears at  $z_{\sigma_u, m2}^+$  in bulk region. The whole WJ region is characterized by the “twin-peak” for  $\sigma_u^+$  for all simulated  $Ra$ s.

The scenario of the PWJ conduces to understanding the “twin peaks” of the velocity fluctuation in RB system. Twin-peak of velocity fluctuation is a common feature for turbulent PWJ even at rather low  $Re_{Mz}$ , due to the effect of the outer free-shear layer structures along some overlap of scales (cf. Ref. 46). In RB system, the “outer structure” is the well-organized LSC. Note that, for the boundary layer in RB system, the second peak would not appear unless  $Re$  is sufficiently large. Additionally, the fact that the first peak is larger than the second one is consistent with turbulent PWJs.<sup>46</sup>

To illustrate the similarity of the fluctuation of the horizontal velocity component, the value of  $\sigma_u^+$  is scaled by the inner peak of

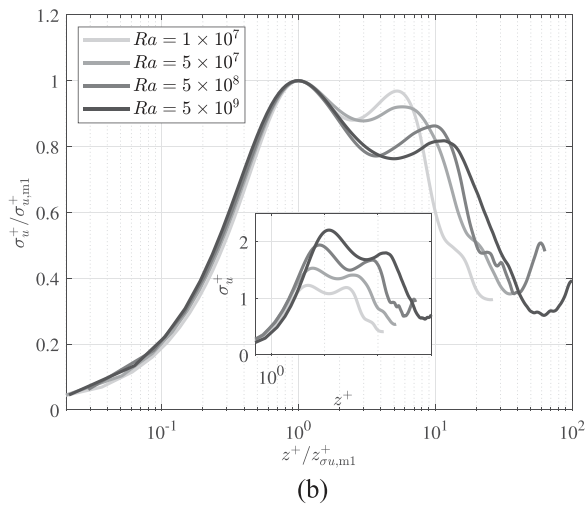
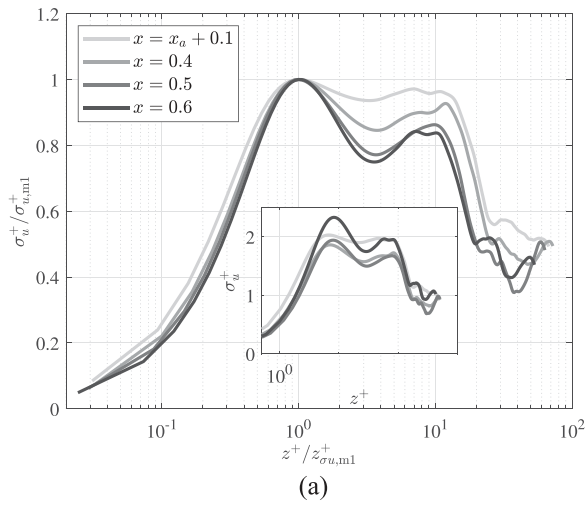


**FIG. 9.** The profiles of horizontal velocity fluctuation  $\sigma_u^+$  normalized by the inner peak  $\sigma_{u,m1}^+$  and the corresponding height  $z_{\sigma_{u,m1}}^+$  at (a) various horizontal locations at  $Ra = 5 \times 10^8$  and (b) various  $Ra$ s at  $x = 0.5$ . The insets are the profiles free from normalization.

$\sigma_{u,m1}^+$  and the wall distance  $z^+$  is normalized with  $z_{\sigma_{u,m1}}^+$ . The similarity of horizontal velocity fluctuation in the inner region,  $z^+ \leq z_{\sigma_{u,m1}}^+$ , is presented with various  $x$  and  $Ra$  in Fig. 9(a) and 9(b), respectively. The inset of Fig. 10(a) shows that  $z_{\sigma_{u,m1}}^+$  seems independent of the horizontal position, and has an  $Ra$ -scaling  $z_{\sigma_{u,m1}}^+ = 0.42Ra^{0.15}$ . The inner peak value  $\sigma_{u,m1}^+$ , on the other hand, presents a “U-shape” along the horizontal direction, as seen in the inset of Fig. 10(b). The strong velocity fluctuation near the stagnation point is associated with intensive plume ejecting at the corner and sweeping downward to the plate thereafter. While the fluid approaching the right sidewall,  $Re_{Mx}$  and adverse pressure gradient for  $x > 0.55$  are largely increased.<sup>10</sup> As a result, the fluctuation increases again at the right corner of the RB cell. Moreover, the horizontal velocity fluctuation at  $x = 0.5$  is approximated as a power law of  $Ra$ ,  $\sigma_{u,m1}^+ = 0.16Ra^{0.125}$ .

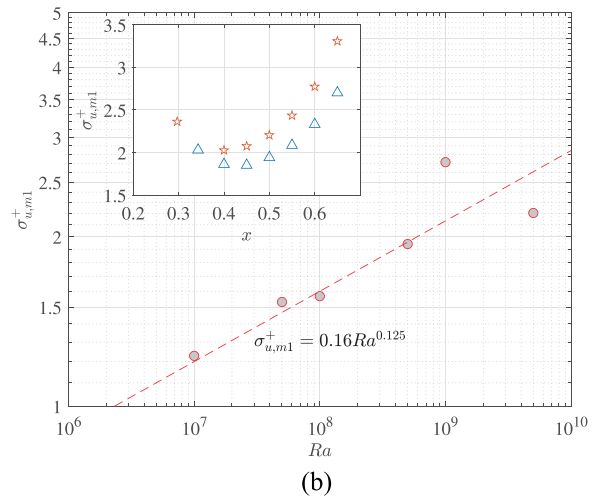
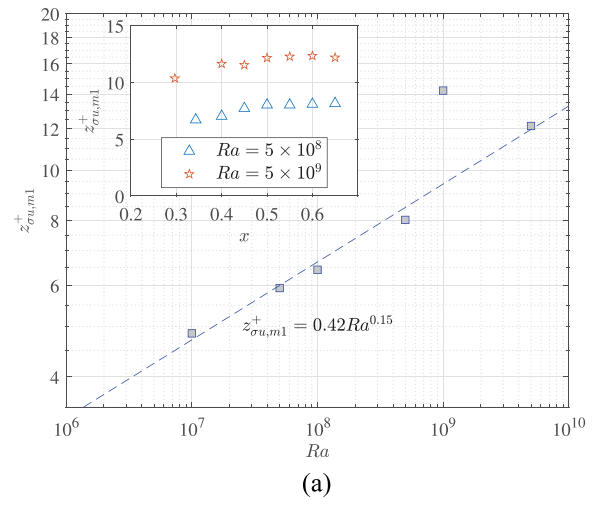


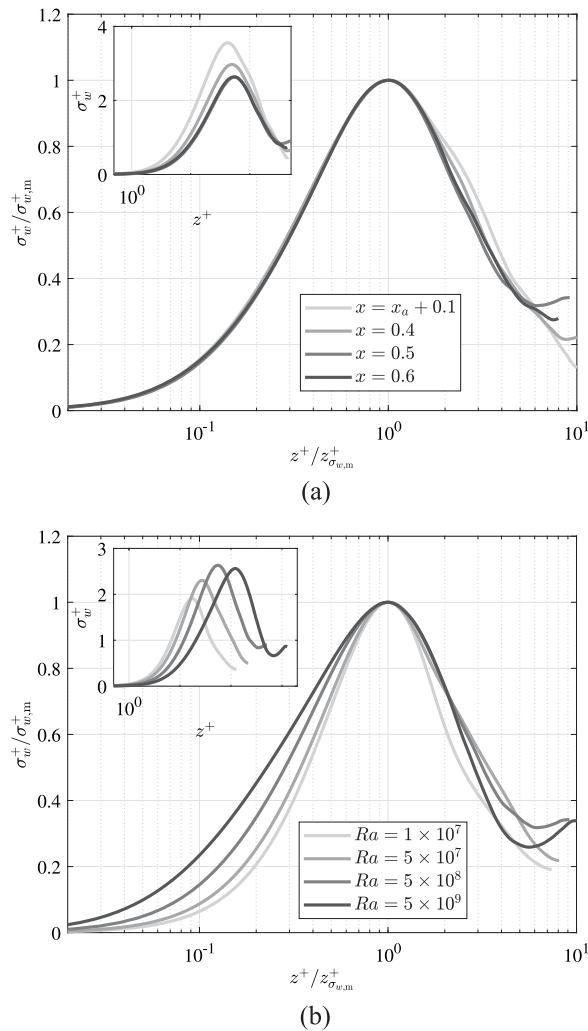
**FIG. 10.** (a) The height of the inner peak of horizontal velocity fluctuation  $z_{\sigma_{u,m1}}^+$  and (b) the magnitude of the fluctuation  $\sigma_{u,m1}^+$  at  $x = 0.5$  as the power functions of  $Ra$ . The insets are variations at different horizontal locations for  $Ra = 5 \times 10^8$  and  $5 \times 10^9$ .

Comparison of the RB and PWJs shows that  $\sigma_{u,m1}^+$  for the RB system is smaller than both the turbulent PWJ ( $\sigma_{u,m1}^+ \approx 3.0$  for  $Re_{Mz} \approx 5000$ )<sup>59</sup> and the turbulent channel (and pipe) flow ( $\sqrt{3.66 + 0.642 \ln Re_\tau}$  and saturates at  $\sqrt{9.2}$ ).<sup>65</sup> Due to the finite  $Ra$  and data scattering, it is hard to distinguish whether  $\sigma_{u,m1}^+$  satisfies square-root-law or power law. If  $\sigma_{u,m1}^+$  satisfies a scaling, it can be extrapolated to  $\sqrt{9.2}$ , and the critical Rayleigh number would be  $1.67 \times 10^{10}$ .

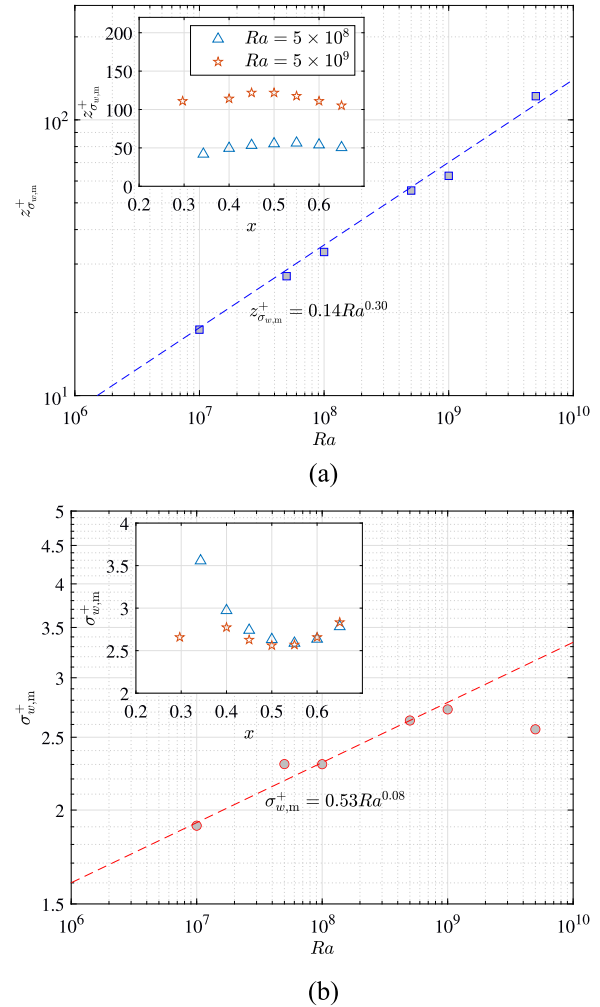
The height of the first peak,  $z_{\sigma_{u,m1}}^+$ , is smaller than that in the turbulent PWJ ( $z_{\sigma_{u,m1}}^+ \approx 20$ – $40$  in Ref. 59), the turbulent channel, and pipe flow ( $z_{\sigma_{u,m1}}^+ \approx 14$  with the direct measurement<sup>66,67</sup> and theoretical value<sup>65</sup>  $z_{\sigma_{u,m1}}^+ = 9.8\sqrt{2}$ ). By extrapolating the scaling of  $z_{\sigma_{u,m1}}^+$  to 14, one has the critical Rayleigh number is about  $1.42 \times 10^{10}$ , consistent with the extrapolation of  $\sigma_{u,m1}^+$ . It implies that the flow is developed turbulence when  $Ra$  is larger than  $1 \times 10^{10}$ .

Figure 11 presents the profiles of  $\sigma_w^+ = \sqrt{w'^2}$  for different horizontal locations and  $Ra$ s normalized with the peak value  $\sigma_{w,m}^+$  and the corresponding scale  $z_{\sigma_{w,m}}^+$ . A peak appears farther away from the wall near  $\sigma_{w,m}^+$ .<sup>68</sup> Figure 11(a) shows the similarity of the vertical profiles of  $\sigma_w^+$  in the range of  $z^+ < z_{\sigma_{w,m}}^+$ . However, it seems that these two scales are not intrinsic for  $Ra$ s, as seen in Fig. 11(b).

The  $Ra$  dependence of  $z_{\sigma_{w,m}}^+$  and  $\sigma_{w,m}^+$  is shown in Fig. 12. The magnitude of  $z_{\sigma_{w,m}}^+$  and  $\sigma_{w,m}^+$  can be approximated as power laws of  $Ra$ , that is,  $z_{\sigma_{w,m}}^+ = 0.14Ra^{0.30}$  and  $\sigma_{w,m}^+ = 0.53Ra^{0.08}$ , respectively. The  $\sigma_{w,m}^+$  grows with increasing  $Ra$ , and the value for the highest  $Ra$  in present cases closes to the value of high  $Re$  WJ ( $\sigma_{w,m}^+ \approx 3$  in Ref. 68) and much higher than those in turbulent pipe and channel flow<sup>65,67</sup> ( $\sigma_{w,m}^+ \approx \sqrt{1.29}$ ), which may be caused by the intensive thermal production near the plate.



**FIG. 11.** The profiles of vertical velocity fluctuation  $\sigma_w^+$  normalized by the peak value  $\sigma_{w,m}^+$  and the corresponding height  $z_{\sigma_{w,m}}^+$  at (a) various horizontal locations at  $Ra = 5 \times 10^8$  and (b) various  $Ra$ s at  $x = 0.5$ . The insets are the profiles free from normalization.



**FIG. 12.** (a) The height of the peak of vertical velocity fluctuation  $z_{\sigma_{w,m}}^+$  and (b) the magnitude of the fluctuation  $\sigma_{w,m}^+$  at  $x = 0.5$  as the power functions of  $Ra$ . The insets are variations at different horizontal locations for  $Ra = 5 \times 10^8$  and  $5 \times 10^9$ .

## F. TKE and dissipation rate

Turbulent transport of RB-WJ is presented by the ratio of the production to dissipation of turbulent energy, as shown in Fig. 13. The turbulence production consists of two parts: shear-induced  $P_s = \overline{u_i' u_j'} \frac{\partial u_i}{\partial x_j}$  and buoyancy-induced  $P_B = \overline{w' \theta'}$ , that is,  $P = P_s + P_B$ .

The dissipation is  $\epsilon = \left( \frac{\partial u_i'}{\partial x_j} \right) \left( \frac{\partial u_i'}{\partial x_j} \right)$ .

The distributions of these variables are qualitatively consistent with TBL<sup>67</sup> and turbulent PWJ.<sup>68</sup> Two peaks of the production are, respectively, located at the edge of the viscous sublayer and the bulk region. In the mixing layer, the turbulence energy is defected and transported from above and below this region.<sup>47</sup> Compared with TBL having a quasi-equilibrium region<sup>67</sup> for  $z^+ > 200$ , the flow in RB system is rather nonequilibrium. The TKE is relatively low in the region

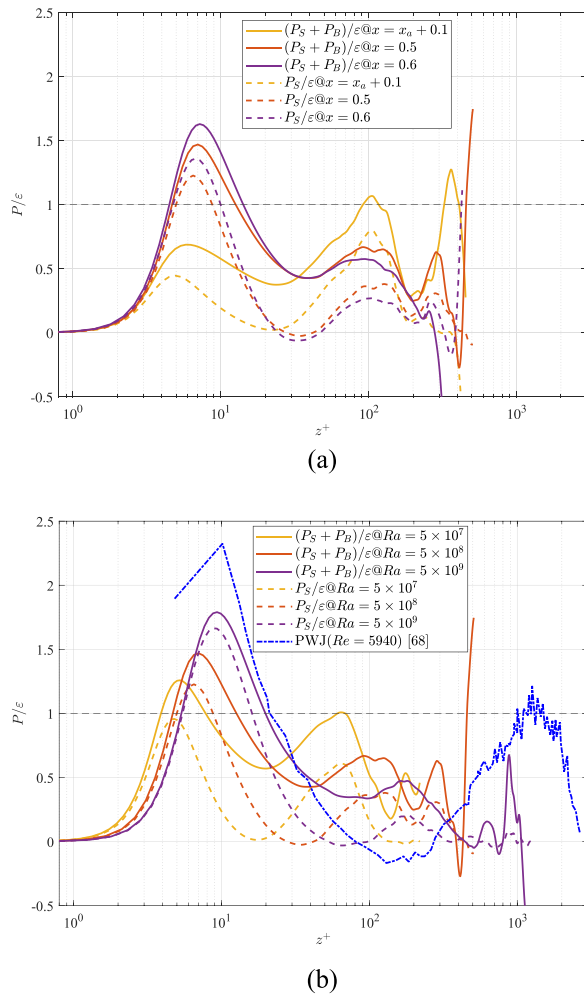


**FIG. 13.** The ratio of turbulent energy production ( $P_s + P_B$  and  $P_s$ ) to dissipation  $\varepsilon$  at (a) various horizontal locations with  $Ra = 5 \times 10^8$  and (b) various  $Ra$  at  $x = 0.5$ . The dashed line of  $P/\varepsilon = 1$  represents the balance between production and dissipation.

near the stagnation point. Due to the well-developed shear, the energy in the stagnation region is supplied by the overflow of upstream plume emission. When the flow develops and  $Ra$  increases,  $P/\varepsilon$  correspondingly increases in the near-wall region but decreases in the bulk. It becomes a distribution more like turbulent PWJ. Moreover, the buoyancy-induced production,  $P_B$ , has a remarkable effect on TKE at moderate  $Ra$ <sup>69,70</sup> in contrast to the shear-induced production,  $P_s$ , dominating the TKE at higher  $Ra$ .

#### IV. HEAT TRANSFER OF RB-WJ

We focus on the heat transfer of the RB-WJ in this section. The mean and rms of temperature profiles are analyzed at various horizontal locations and  $Ra$ s. An OIJ-based heat transfer model is developed to describe the spatial distribution of the Nusselt number on the plate and the scaling law of the maximum Nusselt number ( $Nu_m$ ).

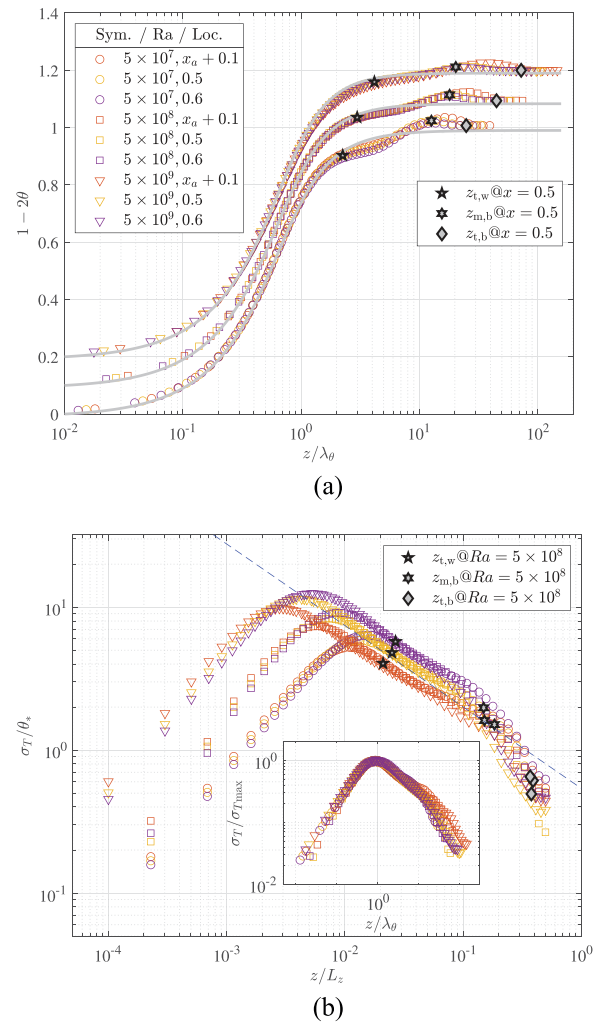


**FIG. 14.** Vertical profiles of mean temperature and temperature fluctuation: (a) mean temperature profiles at various horizontal locations and  $Ra$ s. The gray curves are the thermal BL model proposed by Shishkina *et al.*<sup>71</sup> The curves for each Rayleigh number have been shifted upward with increment of 0.1. (b) Temperature fluctuation (rms) profiles normalized by  $\theta_*$  at various locations and  $Ra$ s. The dashed line is the power law from Refs. 74 and 75,  $\sigma_T/\theta_* = 0.54(z/L_z)^{-0.57}$ . The inset is the temperature fluctuations normalized by their maxima and the height normalized by  $\lambda_\theta$ .

#### A. Self-similar thermal BL solution

The WJ forms a thermal boundary layer on the plate. Figure 14(a) shows the temperature profile at various locations  $x$  with the length scale normalized by the thermal BL thickness  $\lambda_\theta = L_z/(2Nu_x)$ . The temperature within  $z/\lambda_\theta < 4$  is described by the self-similar thermal BL equation with sublayer fluctuation proposed by Shishkina *et al.*<sup>71</sup>

$$\theta = \int_0^{\xi} (1 + a^3 \xi^3)^{-c} d\eta, \quad (19)$$

where  $a = \sqrt[3]{\frac{w'\theta}{\kappa\partial\theta/\partial z}}/\xi = \Gamma(1/3)\Gamma(c - 1/3)/(3\Gamma(c))$  is the coefficient of eddy thermal diffusivity in the thermal sublayer. The



coefficient  $a$  weakly decreases with  $Ra$ , from 1.34 at  $Ra = 1 \times 10^7$  to 1.24 at  $Ra = 5 \times 10^9$ . We note that the model from Shishkina *et al.*<sup>71</sup> was derived under the assumption of thermal BL nested within the viscous BL, that is,  $Pr \geq 1$ , and empirically obtained  $a \sim 1.2$  for  $Pr \approx 1$ . As  $Pr$  in the present study is slightly smaller than unity, the extrapolation of the original model in the manner of Ref. 72 is performed here, without introducing other parameters. Note that the error of the model becomes remarkable at the edge of the thermal BL.

Wellness of the thermal BL model for  $z/\lambda_\theta < 4$  indicates that the thermal BL formed by the WJ is well developed in the region below  $z_{t,w}$ .<sup>43,73</sup> The inset of Fig. 14(a) shows that the temperature residue exists outside  $z_{t,w}$ , though it is used to be considered uniform in RBC. The uneven temperature profile in the bulk region has been observed by Zhou *et al.*<sup>29</sup> We marked the critical positions of  $z_{t,w}$ ,  $z_{m,b}$  and  $z_{t,b}$  in Fig. 14. One can see that they have a close correlation with the temperature profile, indicating that the residue outside the thermal BL is mainly induced by the WJ flow.

The temperature fluctuation (rms) profiles,  $\sigma_T$ , at various  $Ra$ s are shown in Fig. 14(b). The fluctuation of temperature is normalized by convective temperature  $\theta_* = Nu_x^{2/3} Ra^{-1/3} Pr^{-1/3} \Delta T$  as suggested by Deardorff,<sup>76</sup> He and Xia,<sup>74</sup> and Xie *et al.*<sup>75</sup> The length is scaled by the height of the cell  $L_z$ . The location,  $z_{t,w}$ , is marked in the figure representing the thickness of the mixing layer. The profile at the central line [ $x=0.5$ , red symbol in Fig. 14(b)] is consistent with the result from He *et al.*,  $\sigma_T/\theta_* = 0.54(z/L_z)^{-0.57}$ . The power law distribution of  $\sigma_T$  consistent with Adrian's theory<sup>77</sup> is derived from the assumption of matching fluctuating velocities of the bulk region and mixing layer. For the inner scale, the  $\sigma_T$  is normalized by maximal temperature fluctuation,  $\sigma_{T,max}$ , and the length scale normalized by  $\lambda_\theta$  suggested by Wang *et al.*<sup>78,79</sup> The inset of Fig. 14(b) shows that the similarity of thermal fluctuation exists within  $\lambda_\theta$  over the WJ region for all simulated  $Ra$ s.

## B. Approximation of heat transfer distribution

The local Nusselt number on the plate,  $Nu_x$ , is calculated to examine the effect of the OIJ on heat transfer near the plate. Figure 15(a) demonstrates the local heat flux on the bottom conducting plate. It shows that the jet impinging at an angle on the left side of the conducting plate forms an asymmetrical heat flux distribution. The heat flux in the region of the WJ exhibits a similar trend as that in the corner roll. On the WJ side, the heat flux decreases while moving away from the stagnation point. Heat transfer in this region is attributed to the LSC sweeping over the plate where the fluid follows the path on the flat plate. Outside this region near the vertical wall, the heat flux exhibits a similar trend due to the existence of CR, as seen in Fig. 1(a). It is noteworthy that the vortices at  $x < 0.3$  also play a role in heat transfer at corners. The influence of CR on heat transfer in RBC has been investigated by Zhou *et al.* in Ref. 29.

Figure 15(b) shows the time-averaged heat flux in dimensionless form along the horizontal midline at different Rayleigh numbers. The convective motions are strong near the sidewalls due to uprising plumes. Thermal plumes are hardly seen at the cell center, and hence, the convective heat transfer is weak there. Due to the sweeping effect of the large-scale circulation, hot plumes fall downward and cold plumes rise near the sidewalls; therefore, negative heat transfer might occur herein.

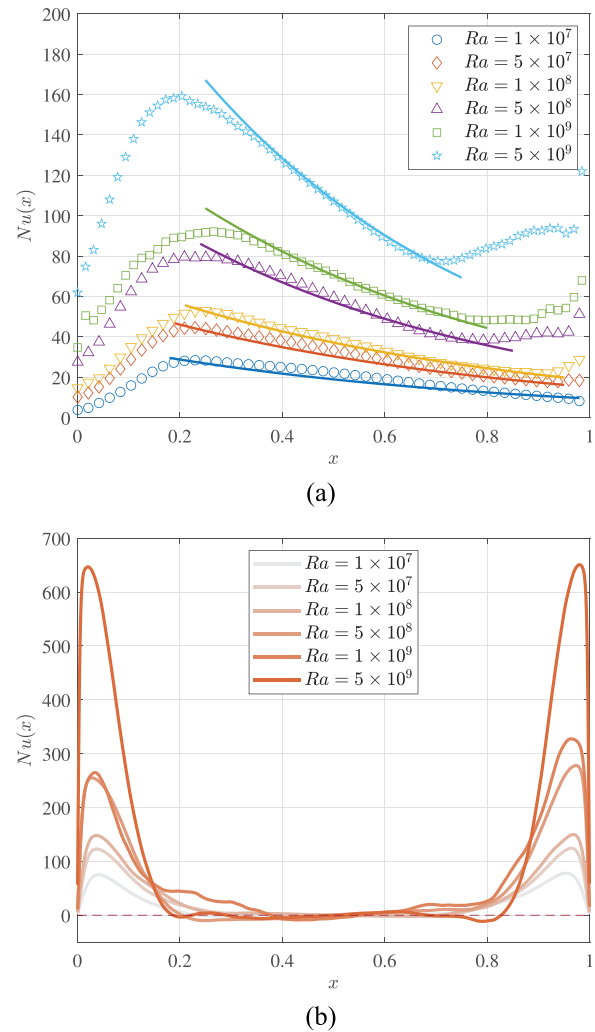


**FIG. 15.** The local Nusselt number  $Nu_x$  (a) at the bottom plate  $z=0$  and (b) at the middle height  $z=0.5$  with various  $Ra$ s. The solid curves in (a) are the results of Eq. (20).

The horizontal distribution of the heat transfer on the plate can be described by an exponential function

$$Nu_x = Nu_m e^{-\tilde{x}}, \quad (20)$$

where  $\tilde{x} = \Delta x/L_w$ ,  $Nu_m$  is the maximum Nusselt number on the plate,  $\Delta x = x - x_{a0}$ , and  $L_w = L_x - x_{a0} - \Delta x_{ej}$ , where  $\Delta x_{ej}$  is the width of the plume ejecting region at the right corner of the RB cell. The parameter  $x_{a0}$  is found to be a constant  $x_{a0} = 0.282$  for the simulated Rayleigh numbers. The Nusselt number as a function of the streamwise location is then approximated as the exponential function of Eq. (20). The error of the function is not more than 15.3%, as seen in Fig. 15(a).

The exponential decay in  $x$ -direction near the stagnation points is equivalent to the exponential growth of thermal BL. The development of the thermal BL is consistent with the similarity analysis of BL

by Cantwell<sup>80</sup> and Shishkina *et al.*<sup>71</sup> On the other hand, Goldstein *et al.* have proposed an empirical formula in form of an exponential function in studying OIJ,<sup>37</sup>

$$Nu = ARe^{0.7} e^{-(B+C \cos \theta_i)(r/D)^n}, \quad (21)$$

where  $D$  is the width of the jet,  $\theta_i$  is the impinging angle, and  $A$ ,  $B$ ,  $C$ ,  $n$  are parameters. For the turbulent OIJ, the empirical values are  $A = 0.107$ ,  $B = 0.47$ ,  $C = 0.23$ , and  $n = 0.75$  for the distance from the jet nozzle to the surface  $L_0/D = 10$ . Here, only two parameters for RBC need to be determined, that is, the stagnation point heat transfer  $Nu_m$  and the length scale  $L_w$  to characterize the OIJ in RBC. Those two parameters should be related to  $Ra$  or  $Re$ , and need more data to examine the influence.

The scenario of OIJ makes it possible to understand the  $Nu_x$  distribution. Figure 15(a) shows that  $Nu$  decreases in the wind direction, which seems to conflict with the view of forced convective BL. For TBL, the heat flux is closely associated with the shearing on the plate. As the flow develops, the shearing is strengthened, and thus,  $Nu$  increases. However, due to the WJ being induced by OIJ, the jet impingement at the stagnation point dominates heat transfer rather than local shear stress, and the heat flux decays as the fluid convecting downstream.

### C. Derivation of maximum Nusselt number

Equation (20) shows that the heat transfer is characterized by the stagnation heat transfer  $Nu_m$ . The relation between  $Nu_m$  and  $Ra$  number is derived by scaling analysis of the temperature equation for OIJ in this section. The temperature equation with respect to the WJ-formed thermal BL is as follows:

$$u \frac{\partial \theta}{\partial x} \sim \kappa \frac{\partial^2 \theta}{\partial z^2}. \quad (22)$$

The left side of the above equation is convection term, in which the velocity is the characteristic velocity of OIJ,  $U_{m,b}$ , as discussed in Sec. III. The length scale in horizontal direction is similar to the scale of slip line (or the scale of CR),  $r_{cr}$ . The right side of the equation is the diffusion term with the scale of thermal BL,  $\lambda_\theta$ . It is interpreted that the convection term  $\frac{U_{m,b} \Delta T / 2 - 0}{r_{cr}}$  represents the heat flux of OIJ passing through the slip line, impinging onto the plate and dissipating in the thermal BL. Based on this fact, we have

$$\frac{U_{m,b}}{r_{cr}} \sim \kappa \frac{1}{\lambda_\theta^2} \quad (23)$$

and

$$\begin{aligned} Nu &= \frac{L_z}{2\lambda_\theta} \sim \frac{1}{2} \sqrt{\frac{U_{m,b} L_z^2}{\kappa r_{cr}}} \\ &= \frac{1}{\sqrt{2}} Re_{lsc}^{1/2} Pr^{1/2} (r_{cr}/L_z)^{-1/2}. \end{aligned} \quad (24)$$

The Reynolds number of LSC,  $Re_{lsc} = U_{m,b} L_z / (2\nu)$ , is estimated by  $Re_m$  in Eq. (7) and  $Re_{lsc} \sim Ra^{0.50}$ . On the other hand, the scaling of the CR size,  $r_{cr}/L_z \sim Ra^{-0.085}$ , was suggested in Ref. 29. Finally, we have

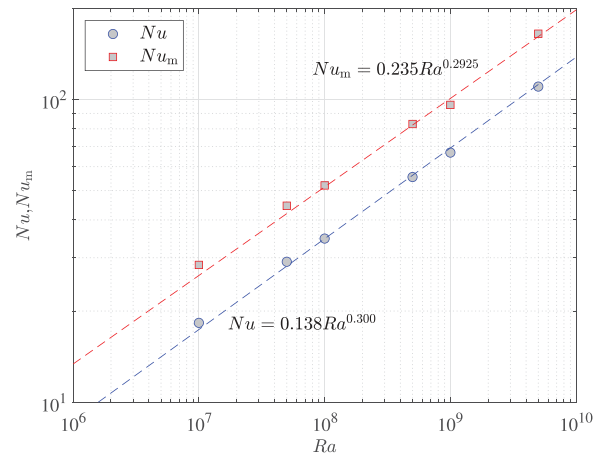


FIG. 16. The maximum Nusselt number  $Nu_m$  and the global Nusselt number  $Nu$  as the power functions of  $Ra$ . The red dashed line is the scaling law for  $Nu_m$  as described by Eq. (25), and the blue dashed line is the scaling law for  $Nu$ .

$$Nu_m \sim Re_m^{1/2} (r_{cr}/L_z)^{-1/2} \sim Ra^{0.2925}. \quad (25)$$

Figure 16 shows that  $Nu_m$  of DNS is in agreement with the scaling model. Note that the relation between  $Nu$  and  $Re$  with regard to the scale of CR gives an effective exponent 0.585 larger than 0.5 in Ref. 81, but smaller than both the impinging jet (0.7) in Ref. 37 and TBL (0.8). This indicates that within the range of the simulated Rayleigh numbers, the impinging jet is still under development throughout the domain. Furthermore,  $Nu_m$  and the global  $Nu$  have the same scaling<sup>14,82</sup> as seen in Fig. 16. This indicates that the WJ characterizes the flow near the plate, and the global  $Nu$  is determined by the heat transfer of the WJ.

### V. CONCLUSIONS

In this paper, an oblique impinging jet is found to dominate momentum and heat transfer on the plate in the Rayleigh–Bénard convection. The OIJ originates from the plume-emission region and contains abundant cold/warm fluid, which drives the motion of LSC. When the jet impingement occurs, the flow develops into a wall jet. The knowledge of turbulent plane wall jet is conducive to understanding both the oblique impinging jet and the wall jet of RBC.

We found that the wall jet in the RB system conforms to the nature of the turbulent plane wall jet along with finite Reynolds number effects. The similarity of the velocity along the plate indicates the coherent motion of the wall jet, which consists of three layers, respectively, called the viscous sublayer, the mixing layer, and the bulk. The layers are, respectively, scaled by the wall friction velocity  $u_\tau$  and the wall unit for the viscous sublayer, the first peak velocity  $U_{m,b}$  and the half-height  $z_{t,b}$  for the bulk, the second peak velocity  $U_{m,w}$ , and its height  $z_{t,w}$  for the mixing layer. The characteristic parameters,  $U_{m,w}$ ,  $z_{t,w}$ , and  $u_\tau$ , being normalized by the local momentum rate  $M_w$ , preserve power laws with  $Ra$  as they are in turbulent plane wall jet.

The streamwise similarity of the thermal boundary layer in the wall jet region is analyzed, and the temperature profiles are well described by the thermal boundary layer model from Shishkina for  $z < 4\lambda_\theta$ . Further analysis reveals that the heat transfer exponentially decays in  $x$ -direction,  $Nu_x = Nu_m \exp(-\tilde{x})$ . We derived the power

law of the maximum  $Nu$  with  $Ra$  by scaling analysis,  $Nu_m \sim Ra^{0.2925}$ , consistent with DNS.

The oblique impinging jet and the wall jet provide insights into the nature of inhomogeneous heat transfer of a turbulent RB system. The second peak of horizontal velocity fluctuation  $\sigma_u^+$  is the property of turbulent plane wall jet, and the temperature residue in the wind-shearing region is attributed to the bulk flow. The occurrence of the maximum heat transfer is interpreted as the result of the energy-containing oblique jet impinging on the plate. The exponential decay of heat transfer along the plate is the nature of the wall jet in the RB system. All results indicate that the near-wall flow and heat transfer of turbulent RBC at moderate Rayleigh numbers depend on the behaviors of the oblique impinging jet and the wall jet.

## ACKNOWLEDGMENTS

We offer our special thanks to Professor Zhen-Su She and Professor Yun Bao for helpful comments and suggestions, and thank Dr. Hong-Yue Zou and Dr. Yan-Guang Yang for their support of the computational work. This work was supported by National Nature Science (China) Fund Nos. 91952201, 11452002, 11521091, and 11372362, and by MOST (China) 973 Project No. 2009CB724100.

## DATA AVAILABILITY

The data that support the findings of this study are available from the corresponding author upon reasonable request.

## REFERENCES

- <sup>1</sup>D. P. McKenzie, J. M. Roberts, and N. O. Weiss, "Convection in the earth's mantle: Towards a numerical simulation," *J. Fluid Mech.* **62**, 465–538 (1974).
- <sup>2</sup>H. Hattori and Y. Nagano, "Direct numerical simulation of turbulent heat transfer in plane impinging jet," *Int. J. Heat Fluid Flow* **25**, 749–758 (2004).
- <sup>3</sup>H. J. Gramberg, P. D. Howell, and J. R. Ockendon, "Convection by a horizontal thermal gradient," *J. Fluid Mech.* **586**, 41–57 (2007).
- <sup>4</sup>M. K. Verma, *Physics of Buoyant Flows: From Instabilities to Turbulence* (World Scientific, 2018).
- <sup>5</sup>T. Zürner, "Refined mean field model of heat and momentum transfer in magnetoconvection," *Phys. Fluids* **32**, 107101 (2020).
- <sup>6</sup>S. Bhattacharya, M. K. Verma, and R. Samtaney, "Revisiting Reynolds and Nusselt numbers in turbulent thermal convection," *Phys. Fluids* **33**, 015113 (2021).
- <sup>7</sup>L. P. Kadanoff, "Turbulent heat flow: Structures and scaling," *Phys. Today* **54** (8), 34 (2001).
- <sup>8</sup>X.-L. Qiu and P. Tong, "Large-scale velocity structures in turbulent thermal convection," *Phys. Rev. E* **64**, 036304 (2001).
- <sup>9</sup>K. R. Sreenivasan, A. Bershadskii, and J. J. Niemela, "Mean wind and its reversal in thermal convection," *Phys. Rev. E* **65**, 056306 (2002).
- <sup>10</sup>H.-Y. Zou, W.-F. Zhou, X. Chen, Y. Bao, J. Chen, and Z.-S. She, "Boundary layer structure in turbulent Rayleigh–Bénard convection in a slim box," *Acta Mech. Sin.* **35**, 713–728 (2019).
- <sup>11</sup>A. Xu, L. Shi, and H.-D. Xi, "Statistics of temperature and thermal energy dissipation rate in low-Prandtl number turbulent thermal convection," *Phys. Fluids* **31**, 125101 (2019).
- <sup>12</sup>A. Xu, X. Chen, F. Wang, and H.-D. Xi, "Correlation of internal flow structure with heat transfer efficiency in turbulent Rayleigh–Bénard convection," *Phys. Fluids* **32**, 105112 (2020).
- <sup>13</sup>V. T. Vishnu, A. K. De, and P. K. Mishra, "Dynamics of large-scale circulation and energy transfer mechanism in turbulent Rayleigh–Bénard convection in a cubic cell," *Phys. Fluids* **32**, 095115 (2020).
- <sup>14</sup>S. Grossmann and D. Lohse, "Scaling in thermal convection: A unifying theory," *J. Fluid Mech.* **407**, 27–56 (2000).
- <sup>15</sup>T. Wei and R. du Puits, "Inner and outer scales in turbulent Rayleigh–Bénard convection," *Phys. Fluids* **32**, 115115 (2020).
- <sup>16</sup>J. Chen, Y. Bao, Z.-X. Yin, and Z.-S. She, "Theoretical and numerical study of enhanced heat transfer in partitioned thermal convection," *Int. J. Heat Mass Transfer* **115**, 556–569 (2017).
- <sup>17</sup>Y. Bao, J. Chen, B.-F. Liu, Z.-S. She, J. Zhang, and Q. Zhou, "Enhanced heat transport in partitioned thermal convection," *J. Fluid Mech.* **784**, R5 (2015).
- <sup>18</sup>K. L. Chong, S. D. Huang, M. Kaczorowski, and K.-Q. Xia, "Condensation of coherent structures in turbulent flows," *Phys. Rev. Lett.* **115**, 264503 (2015).
- <sup>19</sup>K. L. Chong and K.-Q. Xia, "Exploring the severely confined regime in Rayleigh–Bénard convection," *J. Fluid Mech.* **805**, R4 (2016).
- <sup>20</sup>K. L. Chong, Y. Yang, S. D. Huang, J.-Q. Zhong, R. J. Stevens, R. Verzicco, D. Lohse, and K. Q. Xia, "Confined Rayleigh–Bénard, rotating Rayleigh–Bénard, and double diffusive convection: A unifying view on turbulent transport enhancement through coherent structure manipulation," *Phys. Rev. Lett.* **119**, 064501 (2017).
- <sup>21</sup>S.-D. Huang and K.-Q. Xia, "Effects of geometric confinement in quasi-2D turbulent Rayleigh–Bénard convection," *J. Fluid Mech.* **794**, 639–654 (2016).
- <sup>22</sup>J.-L. Yang, Y.-Z. Zhang, T. C. Jin, Y.-H. Dong, B.-F. Wang, and Q. Zhou, "The Pr-dependence of the critical roughness height in two-dimensional turbulent Rayleigh–Bénard convection," *J. Fluid Mech.* **911**, 1091 (2021).
- <sup>23</sup>Y.-Z. Zhang, C. Sun, Y. Bao, and Q. Zhou, "How surface roughness reduces heat transport for small roughness heights in turbulent Rayleigh–Bénard convection," *J. Fluid Mech.* **836**, 786 (2018).
- <sup>24</sup>D.-L. Dong, B.-F. Wang, Y.-H. Dong, Y.-X. Huang, N. Jiang, Y.-L. Liu, Z.-M. Lu, X. Qiu, Z.-Q. Tang, and Q. Zhou, "Influence of spatial arrangements of roughness elements on turbulent Rayleigh–Bénard convection," *Phys. Fluids* **32**, 045114 (2020).
- <sup>25</sup>B.-F. Wang, Q. Zhou, and C. Sun, "Vibration-induced boundary-layer destabilization achieves massive heat-transport enhancement," *Sci. Adv.* **6**, eaaz8239 (2020).
- <sup>26</sup>R. Yang, K. L. Chong, Q. Wang, R. Verzicco, O. Shishkina, and D. Lohse, "Periodically modulated thermal convection," *Phys. Rev. Lett.* **125**, 154502 (2020).
- <sup>27</sup>Z. Wang, V. Mathai, and C. Sun, "Self-sustained biphasic catalytic particle turbulence," *Nat. Commun.* **10**, 3333 (2019).
- <sup>28</sup>K.-Q. Xia, C. Sun, and S.-Q. Zhou, "Particle image velocimetry measurement of the velocity field in turbulent thermal convection," *Phys. Rev. E* **68**, 066303 (2003).
- <sup>29</sup>W. F. Zhou and J. Chen, "Letter: Similarity model for corner roll in turbulent Rayleigh–Bénard convection," *Phys. Fluids* **30**, 111705 (2018).
- <sup>30</sup>E. P. van der Poel, R. Verzicco, S. Grossmann, and D. Lohse, "Plume emission statistics in turbulent Rayleigh–Bénard convection," *J. Fluid Mech.* **772**, 5–15 (2015).
- <sup>31</sup>G. Ahlers, E. Bodenschatz, and D. Funfschilling, "Logarithmic temperature profiles in turbulent Rayleigh–Bénard convection," *Phys. Rev. Lett.* **109**, 114501 (2012).
- <sup>32</sup>G. Ahlers, E. Bodenschatz, and X. He, "Logarithmic temperature profiles of turbulent Rayleigh–Bénard convection in the classical and ultimate state for a Prandtl number of 0.8," *J. Fluid Mech.* **758**, 436–467 (2014).
- <sup>33</sup>S. Wagner, O. Shishkina, and C. Wagner, "Boundary layers and wind in cylindrical Rayleigh–Bénard cells," *J. Fluid Mech.* **697**, 336–366 (2012).
- <sup>34</sup>R. Kaiser and R. du Puits, "Local wall heat flux in confined thermal convection," *Int. J. Heat Mass Transfer* **73**, 752–760 (2014).
- <sup>35</sup>Q. Zhou, K. Sugiyama, R. J. A. M. Stevens, S. Grossmann, D. Lohse, and K. Xia, "Horizontal structures of velocity and temperature boundary layers in two-dimensional numerical turbulent Rayleigh–Bénard convection," *Phys. Fluids* **23**, 125104 (2011).
- <sup>36</sup>Q. Zhou and K.-Q. Xia, "Thermal boundary layer structure in turbulent Rayleigh–Bénard convection in a rectangular cell," *J. Fluid Mech.* **721**, 199–224 (2013).
- <sup>37</sup>R. J. Goldstein and M. E. Franchett, "Heat transfer from a flat surface to an oblique impinging jet," *J. Heat Transfer* **110**, 84–90 (1988).
- <sup>38</sup>B. E. Launder and W. Rodi, "The turbulent wall jet measurements and modeling," *Annu. Rev. Fluid Mech.* **15**, 429–459 (1983).
- <sup>39</sup>M. B. Glauert, "The wall jet," *J. Fluid Mech.* **1**, 625 (1956).

- <sup>40</sup>R. Narasimha, K. Y. Narayan, and S. Parthasarathy, "Parametric analysis of turbulent wall jets in still air," *Aeronaut. J.* **77**, 355 (1973).
- <sup>41</sup>A. Gupta, H. Choudhary, A. K. Singh, T. Prabhakaran, and S. A. Dixit, "Scaling mean velocity in two-dimensional turbulent wall jets," *J. Fluid Mech.* **891**, 132 (2020).
- <sup>42</sup>G. E. Myers, J. J. Schauer, and R. H. Eustis, "Closure to 'Discussion of 'Plane turbulent wall jet flow development and friction factor'" (1963, ASME J. Basic Eng., 85, pp. 53–54)," *J. Basic Eng.* **85**, 54–54 (1963).
- <sup>43</sup>K. Gersten, "The asymptotic downstream flow of plane turbulent wall jets without external stream," *J. Fluid Mech.* **779**, 351–370 (2015).
- <sup>44</sup>I. Wygnanski, Y. Katz, and E. Horev, "On the applicability of various scaling laws to the turbulent wall jet," *J. Fluid Mech.* **234**, 669–690 (1992).
- <sup>45</sup>B. E. Launder, "The turbulent wall jet," *Prog. Aerosp. Sci.* **19**, 81–128 (1979).
- <sup>46</sup>S. Bhatt and E. Gnanamanickam, "Linear and nonlinear mechanisms within a forced plane wall jet," *Phys. Rev. Fluids* **5**, 074604 (2020).
- <sup>47</sup>A. Dejoan and M. A. Leschziner, "Large eddy simulation of a plane turbulent wall jet," *Phys. Fluids* **17**, 025102 (2005).
- <sup>48</sup>W. K. George, H. Abrahamsson, J. Eriksson, R. I. Karlsson, L. Löfdahl, and M. Wosnik, "A similarity theory for the turbulent plane wall jet without external stream," *J. Fluid Mech.* **425**, 367–411 (2000).
- <sup>49</sup>G. I. Barenblatt, A. J. Chorin, and V. M. Prostokishin, "The turbulent wall jet: A triple-layered structure and incomplete similarity," *Proc. Natl. Acad. Sci.* **102**, 8850–8853 (2005).
- <sup>50</sup>R. Verzicco and P. Orlandi, "A finite-difference scheme for three-dimensional incompressible flows in cylindrical coordinates," *J. Comput. Phys.* **123**, 402–414 (1996).
- <sup>51</sup>R. Verzicco and R. Camussi, "Numerical experiments on strongly turbulent thermal convection in a slender cylindrical cell," *J. Fluid Mech.* **477**, 19 (2003).
- <sup>52</sup>R. J. A. M. Stevens, D. Lohse, and R. Verzicco, "Prandtl and Rayleigh number dependence of heat transport in high Rayleigh number thermal convection," *J. Fluid Mech.* **688**, 31–43 (2011).
- <sup>53</sup>O. Shishkina, R. J. Stevens, S. Grossmann, and D. Lohse, "Boundary layer structure in turbulent thermal convection and its consequences for the required numerical resolution," *New J. Phys.* **12**, 075022 (2010).
- <sup>54</sup>J. J. Niemela and K. R. Sreenivasan, "Confined turbulent convection," *J. Fluid Mech.* **481**, 355–384 (2003).
- <sup>55</sup>S. Grossmann and D. Lohse, "Prandtl and Rayleigh number dependence of the Reynolds number in turbulent thermal convection," *Phys. Rev. E* **66**, 016305 (2002).
- <sup>56</sup>C. Sun and K.-Q. Xia, "Scaling of the Reynolds number in turbulent thermal convection," *Phys. Rev. E* **72**, 067302 (2005).
- <sup>57</sup>S. A. Dixit, A. Gupta, H. Choudhary, A. K. Singh, and T. Prabhakaran, "Asymptotic scaling of drag in flat-plate turbulent boundary layers," *Phys. Fluids* **32**, 041702 (2020).
- <sup>58</sup>W. H. Schwarz and W. P. Cosart, "The two-dimensional turbulent wall-jet," *J. Fluid Mech.* **10**, 481 (1961).
- <sup>59</sup>J. G. Eriksson, R. I. Karlsson, and J. Persson, "An experimental study of a two-dimensional plane turbulent wall jet," *Exp. Fluids* **25**, 50–60 (1998).
- <sup>60</sup>H. A. P. Irwin, "Measurements in a self-preserving plane wall jet in a positive pressure gradient," *J. Fluid Mech.* **61**, 33–63 (1973).
- <sup>61</sup>The origin value 0.74 is based on the normalized height is half-height and transform to 4.93 by multiplying the ratio of half-height to position of velocity inner peak.
- <sup>62</sup>G. I. Barenblatt, *Scaling, Self-Similarity and Intermediate Asymptotics* (Cambridge University Press, 1996).
- <sup>63</sup>P. Bradshaw and M. T. Gee, *Turbulent Wall Jets With and Without An External Stream* (Her Majesty's Stationery Office, 1962).
- <sup>64</sup>Z.-S. She, X. Chen, and F. Hussain, "Quantifying wall turbulence via a symmetry approach: A Lie group theory," *J. Fluid Mech.* **827**, 322–356 (2017).
- <sup>65</sup>X. Chen, F. Hussain, and Z.-S. She, "Quantifying wall turbulence via a symmetry approach. Part 2. Reynolds stresses," *J. Fluid Mech.* **850**, 401–438 (2018).
- <sup>66</sup>S. B. Pope, *Turbulent Flows* (Cambridge University Press, 2000).
- <sup>67</sup>M. Lee and R. D. Moser, "Direct numerical simulation of turbulent channel flow up to  $Re_\tau \approx 5200$ ," *J. Fluid Mech.* **774**, 395–415 (2015).
- <sup>68</sup>E. P. Gnanamanickam, S. Bhatt, S. Artham, and Z. Zhang, "Large-scale motions in a plane wall jet," *J. Fluid Mech.* **877**, 239–281 (2019).
- <sup>69</sup>R. Togni, A. Cimarelli, and E. D. Angelis, "Physical and scale-by-scale analysis of Rayleigh–Bénard convection," *J. Fluid Mech.* **782**, 380–404 (2015).
- <sup>70</sup>R. Togni, A. Cimarelli, and E. D. Angelis, "Resolved and subgrid dynamics of Rayleigh–Bénard convection," *J. Fluid Mech.* **867**, 906–933 (2019).
- <sup>71</sup>O. Shishkina, S. Horn, S. Wagner, and E. S. C. Ching, "Thermal boundary layer equation for turbulent Rayleigh–Bénard convection," *Phys. Rev. Lett.* **114**, 114302 (2015).
- <sup>72</sup>O. Shishkina, S. Horn, M. S. Emran, and E. S. C. Ching, "Mean temperature profiles in turbulent thermal convection," *Physical Review Fluids* **2**(11), 113502 (2017).
- <sup>73</sup>N. Afzal, "Analysis of power law and log law velocity profiles in the overlap region of a turbulent wall jet," *Proc. R. Soc. A* **461**, 1889–1910 (2005).
- <sup>74</sup>Y.-H. He and K.-Q. Xia, "Temperature fluctuation profiles in turbulent thermal convection: A logarithmic dependence versus a power-law dependence," *Phys. Rev. Lett.* **122**, 014503 (2019).
- <sup>75</sup>Y.-C. Xie, B.-Y.-C. Cheng, Y.-B. Hu, and K.-Q. Xia, "Universal fluctuations in the bulk of Rayleigh–Bénard turbulence," *J. Fluid Mech.* **878**, 667 (2019).
- <sup>76</sup>J. W. Deardorff, "Convective velocity and temperature scales for the unstable planetary boundary layer and for Rayleigh convection," *J. Atmos. Sci.* **27**, 1211–1213 (1970).
- <sup>77</sup>R. J. Adrian, "Variation of temperature and velocity fluctuations in turbulent thermal convection over horizontal surfaces," *Int. J. Heat Mass Transfer* **39**, 2303–2310 (1996).
- <sup>78</sup>Y. Wang, X. He, and P. Tong, "Boundary layer fluctuations and their effects on mean and variance temperature profiles in turbulent Rayleigh–Bénard convection," *Phys. Rev. Fluids* **1**, 082301 (2016).
- <sup>79</sup>Y. Wang, W. Xu, X. He, H. F. Yik, X. Wang, J. Schumacher, and P. Tong, "Boundary layer fluctuations in turbulent Rayleigh–Bénard convection," *J. Fluid Mech.* **840**, 408–431 (2018).
- <sup>80</sup>B. J. Cantwell, *Introduction to Symmetry Analysis*, 1st ed. (Cambridge University Press, 2002).
- <sup>81</sup>H. Schlichting, K. Gersten, and E. Krause, *Boundary Layer Theory* (Springer, 1968).
- <sup>82</sup>A. Kumar and S. Subudhi, "Thermal fluctuations and boundary layer properties of turbulent natural convection inside open cavities of different dimensions heated from below," *Phys. Fluids* **32**, 067114 (2020).
- <sup>83</sup>K. Narayan and R. Narasimha, "Parametric Analysis of Turbulent Wall Jets," *Aeronautical Quarterly* **24**(3), 207–218 (1973).